

3.01 Metal Fuel

T. Ogata

Central Research Institute of Electric Power Industry, Tokyo, Komae, Japan

© 2012 Elsevier Ltd. All rights reserved.

3.01.1	Introduction	2
3.01.2	Properties of Metal Fuel Alloys	4
3.01.2.1	Physical Properties	4
3.01.2.1.1	Density	4
3.01.2.1.2	Solidus and liquidus temperatures	5
3.01.2.1.3	Phase transition temperatures	6
3.01.2.1.4	Heat capacity	7
3.01.2.1.5	Thermal conductivity	7
3.01.2.1.6	Thermal expansion	8
3.01.2.2	Mechanical Properties	9
3.01.2.3	Diffusion Properties	12
3.01.2.4	Effects of MA Addition	13
3.01.3	Metal Fuel Fabrication	14
3.01.3.1	Fuel Slug Fabrication	15
3.01.3.1.1	Injection casting	15
3.01.3.1.2	Other methods	18
3.01.3.2	Fuel Pin Assembly	19
3.01.4	Steady-State Irradiation Behavior	19
3.01.4.1	Steady-State Irradiation Tests	19
3.01.4.2	Fuel Constituent Migration	20
3.01.4.3	Fission Gas Release and Gas Swelling	21
3.01.4.4	Restructuring and Deformation of the Fuel Slug	25
3.01.4.5	Fuel–Cladding Mechanical Interaction	27
3.01.4.6	Change in Fuel Slug Temperature	28
3.01.4.7	Fuel–Cladding Chemical Interaction	28
3.01.4.8	Behavior of Fission Products	29
3.01.4.9	Behavior of Breached Fuel Pins	30
3.01.4.10	Behavior of MA-Bearing Metal Fuel	31
3.01.4.11	Factors Controlling Fuel Lifetime	31
3.01.5	Transient Behavior	32
3.01.5.1	Transient Tests	32
3.01.5.2	Linear-Power-to-Melting	32
3.01.5.3	Liquefaction at the Fuel–Cladding Interface	33
3.01.5.4	Molten Fuel Motion	35
3.01.5.5	Fuel Pin Failure Mechanism	36
3.01.5.6	Failed Fuel Behavior	37
3.01.6	Summary and Future Development	37
References		37

Abbreviations

ACS	Advanced casting system
AGHCF	Alpha–Gamma Hot Cell Facility
ANL	Argonne National Laboratory
bcc	Body-centered cubic

BCS	Bench-scale casting system
CP-5	Chicago pile No.5 reactor
CRIEPI	Central Research Institute of Electric Power Industry
DN	Delayed neutron

EBR-I, II	Experimental Breeder Reactor-I, II
FBTA	Fuel behavior test apparatus
FCCI	Fuel-cladding chemical interaction
FCF	Fuel cycle facility
FCMI	Fuel-cladding mechanical interaction
FFT	Fast Flux Test Facility
Fs	Fissium, a mixture of metals: 49.2Mo, 39.2Ru, 5.6Rh, 3.8Pd, 2Zr, and 0.2Nb (in wt%)
Fz	Fizzium, a mixture of metals: 27.5Mo, 29.5Ru, 5Rh, 10Pd, and 28Zr (in wt%)
IFR	Integral Fast Reactor
INL	Idaho National Laboratory
KAERI	Korea Atomic Energy Research Institute
LOF	Loss of flow
MA	Minor actinides
RBCB	Run-beyond-cladding breach
RE	Rare earths
SD	Smear density
TOP	Transient overpower
TREAT	Transient reactor test facility
TRU	Transuranium element
UTOP	Unprotected transient overpower
WPF	Whole-pin furnace

3.01.1 Introduction

Metal fuels are ideal for fast reactors because they have higher densities of fissile and fertile materials than any other fuel forms and provide higher reactor core performance such as higher breeding ratio and less fissile inventory. Early experimental fast reactors – Experimental Breeder Reactor I (EBR-I), EBR-II, the Enrico Fermi Reactor, and the Dounreay Fast Reactor (DFR) – therefore utilized uranium alloys as driver fuel. The burnup of metal fuel in those days was limited to a few atom percent (at.%) because of the increase in the fuel–cladding mechanical interaction (FCMI) caused by gas swelling of fuel alloys. Before the full potential of metal fuel was revealed, the global trend of fast reactor fuel development was directed toward oxide fuels. However, continuous efforts were made to raise the burnup limit of driver fuel of the EBR-II at Argonne National Laboratory (ANL) in the United States. It was found that reducing the fuel smear density to about 75% was effective in promoting fission gas release before fuel–cladding contact and in suppressing FCMI at an early stage of irradiation. Here, ‘smear density (%)’ is defined as the cross-sectional area ratio of the fuel slug to the cladding inside. This finding increased the design

burnup limit of the Mk-II driver fuel to 8 at.%. Another issue in metal fuel development at the time was to explore appropriate compositions of Pu-bearing fuel, which is essential in fuel cycle systems for fast breeder reactors. The Mk-I and Mk-II driver fuels of EBR-II were the U–5 wt% Fs alloy, where Fs stands for fissium, a mixture of metals: 2.46Mo, 1.96Ru, 0.28Rh, 0.19Pd, 0.1Zr, and 0.01Nb (in wt%), which is the equilibrium composition of residual materials left in the melt-refining process.¹ Because the U–Pu–Fs alloys showed unsatisfactory compatibility with cladding materials, various other U–Pu-based alloys were examined from the standpoint of physical properties, irradiation performance, and compatibility with cladding materials. As a result, the ANL researchers considered that U–Pu–Zr alloys would be the best because of their solidus temperature and compatibility with stainless steels. The above history of metal fuel development until the 1980s is described in Stevenson,¹ Walters *et al.*,² Hofman and Walters,³ Hofman *et al.*,⁴ and Crawford *et al.*⁵

The key features of metal fuel design – U–Pu–10 wt% Zr fuel slug and ~75% smear density – were embodied in the Integral Fast Reactor (IFR) program^{6,7} initiated at ANL in 1984. A schematic view of a metal fuel is shown in Figure 1. The cylindrical fuel alloy rod is called a ‘fuel slug.’ Because sodium does not react with U–Pu–Zr alloys, the annular gap between the fuel slug and the cladding can be filled with sodium (bond Na) to ensure thermal conduction from the fuel slug to the coolant. A relatively large gas plenum, which is a space above the fuel slug, is provided to mitigate the pressure of the fission gas accumulating in the course of irradiation. In the IFR program, ~2000 test pins of the U–10 wt% Zr binary alloy fuel and ~600 test pins of the U–Pu–10 wt% Zr ternary fuel were irradiated in EBR-II and the Fast Flux Test Facility (FFT)⁸ until the program had to be terminated in 1994. Of these test pins, about 300 U–Pu–Zr pins and 1500 U–Zr pins exceeded 10 at. % burnup.⁸ The highest burnup achieved was more than 19 at.% for the U–19 wt% Pu–10 wt% Zr fuel pin,^{5,9} whereby the high burnup capability of the metal fuel was demonstrated. All of the driver fuel of EBR-II was converted to Mk-III fuel (U–10 wt% Zr), and more than 10 000 U–10 wt% Zr fuel pins were irradiated.⁸ A wide variety of irradiation tests, in-pile transient tests,¹⁰ and out-of-pile heating tests^{11,12} in the IFR program revealed steady-state irradiation behavior and transient performance of metal fuel.

An important factor in selecting a fuel form for fast reactors is ease of fuel recycling, that is,

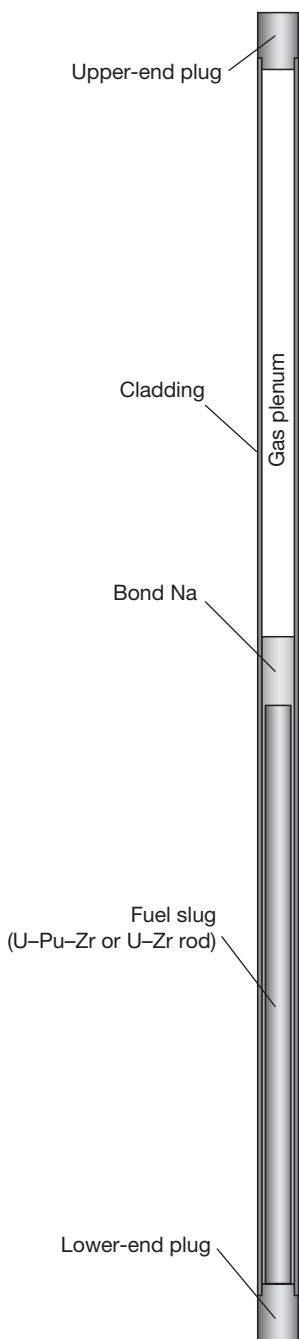


Figure 1 Schematic view of a metal fuel pin.

reprocessing and fuel refabrication. The recycling of metal fuel has already been demonstrated in the 1960s at ANL, although the fuel was the U–5Fs alloy and the burnup was limited to 1.2 at.%.¹ About 560 fuel subassemblies were processed by the low-decontamination pyrometallurgical process, called ‘melt refining,’ and then fuel slugs were refabricated by injection-casting

from the recovered fuel and an additional new alloy.¹ Approximately 34 500 acceptable fuel elements were made remotely in the hot cell in the Fuel Cycle Facility (FCF) adjacent to EBR-II. From these elements, 418 fuel subassemblies were returned to the EBR-II reactor.¹ The fuel alloy was recycled as many as four times, and the fuel was returned to the reactor within 4–6 weeks of its removal from the reactor core.¹ Current fuel cycle technologies for metal fuel – electrometallurgical process and injection casting – were developed in the IFR program. These technologies are expected to reduce the fuel cycle cost even for small-scale fuel cycle plants because of the simplicity of the process and the compactness of the equipment.^{6,7} For example, in the injection-casting process, composition adjustment, melting (alloying), and casting of the fuel slug can be done in a single injection-casting furnace. In the electrometallurgical process, irradiated metal fuel is anodically dissolved. While uranium is deposited on the solid cathode, plutonium is collected in the liquid cadmium cathode with uranium, minor actinides (MA: Np, Am, Cm), and part of the lanthanide fission products, according to thermochemical theory. This inherently low-decontamination aspect brings about a proliferation-resistant feature to the electrometallurgical process.^{6,7}

A recent incentive for fast reactor development is to reduce the repository burden of radioactive waste. This can be achieved by separating long-lived MA from spent light-water reactor fuel, burning MA in fast reactors, and decreasing the long-term radioactivity of nuclear waste. Metal-fueled fast reactors facilitate the effective transmutation of MA because of the high-energy neutron spectrum.^{13,14} One of the measures to load MA into the reactor core is to add MA to the fuel alloy homogeneously. In response to this incentive, recent metal fuel development in the United States has been devoted to MA-bearing fuel. Physical property measurements, irradiation tests, and out-of-pile tests for compatibility with cladding materials are now being conducted at the Idaho National Laboratory (INL).¹⁵

The distinctive features of metal fuel and its fuel cycle have driven metal fuel development in other countries such as Japan and South Korea. The Central Research Institute of Electric Power Industry (CRIEPI) in Japan started metal fuel research in 1986,¹⁶ followed by the Korea Atomic Energy Research Institute (KAERI).¹⁷ Metal fuel research in these organizations includes fuel alloy characterization, fuel performance code development, fuel fabrication technology development, and irradiation tests.

This chapter summarizes the main features of U–Zr and U–Pu–Zr metal fuels, especially their physical and mechanical properties, fabrication technology, steady-state irradiation behavior, and transient behavior. Recent results of MA-bearing metal fuel development are also presented. Finally, future developments are suggested.

3.01.2 Properties of Metal Fuel Alloys

This section summarizes the physical, mechanical, and other properties of U–Zr and U–Pu–Zr alloys that have been reported to date. Many of the property data were reported in the 1960s and 1970s,^{18–26} and some thermal properties were measured in the 1980s.^{27–31} These data, which are not sufficient at this stage, are fundamental to the metal fuel development.

U–Zr binary and U–Pu–Zr ternary phase diagrams^{32,33} are also essential in understanding the characteristics of these alloys, which are summarized in Chapter 2.05, Phase Diagrams of Actinide Alloys along with other actinide alloy phase diagrams.

3.01.2.1 Physical Properties

3.01.2.1.1 Density

The density of cast U–Pu–Zr alloys at room temperature varies linearly with the atom percent (at.%) of Zr in the alloy.²⁰ The density is little affected by the Pu content ranging from 10 to 20 at.%, but decreases with increasing carbon and oxygen impurities.²⁰ The density data measured by Harbur *et al.*²³ also indicate a linear density variation with the Zr content. Other U–Pu–Zr density data are reported in Boucher and Barthelemy.¹⁹ The density of U–Zr alloys can be found in Rough.¹⁸ These published data are summarized in Figure 2. The figure shows fair agreement among the data. Small difference among the data may be attributed to the impurity level and/or the alloy-manufacturing method.

The densities of U–Zr and U–Pu–Zr alloys can be estimated from the molar volumes³⁴ of their respective constituents, assuming the additive law with respect to molar volume. The estimated densities of U–Zr and U–30 at.% Pu–Zr alloys seem to give the upper bound, as shown in Figure 2. The densities at elevated temperatures can be estimated by using thermal expansion data.

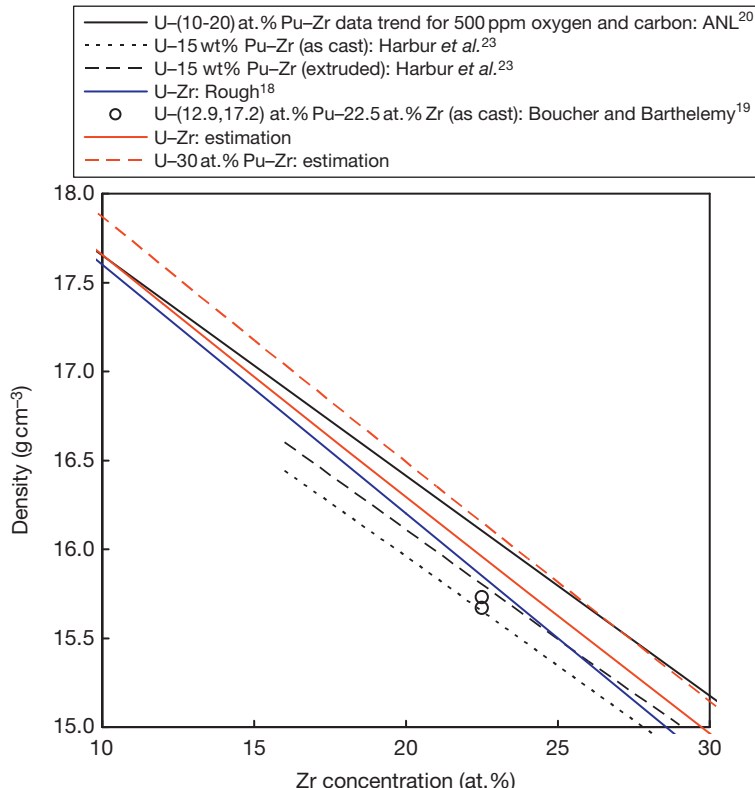


Figure 2 Density of U–Zr and U–Pu–Zr alloys.

Table 1 Solidus and liquidus temperatures of U–Zr and U–Pu–Zr alloys

Ref.	Composition (at.%)	Solidus (K)			Liquidus (K)		
		Data in Ref.	Eqn [1]	Deviation	Data in Ref.	Eqn [2]	Deviation
22	U–10.0Pu–15.0Zr	1393	1396	–3	1473	1553	–80
22	U–12.9Pu–22.5Zr	1428	1426	2	1523	1626	–103
22	U–15.0Pu–30.0Zr	1443	1468	–25	1563	1686	–123
23	U–13.5Pu–16.0Zr	1378±10	1370	8	1513±20	1555	–42
23	U–12.3Pu–29.0Zr	1468±10	1485	–17	1698±20	1686	12
29	U–19.3Zr	1489±7	1541	–52	1631±10	1626	5
29	U–19.5Pu–3.3Zr	1269±5	1234	35	1323±4	1336	–13
29	U–19.3Pu–14.5Zr	1366±8	1310	56	1594±23	1519	75
35	U–24.4Zr		1582		1700	1673	27
35	U–39.3Zr		1709		1793	1793	0

3.01.2.1.2 Solidus and liquidus temperatures

The solidus and liquidus temperatures of U–Pu–Zr alloys have been reported by Kelman *et al.*,²² Harbur *et al.*,²³ and Leibowitz *et al.*²⁹ and those of U–Zr alloys by Leibowitz *et al.*²⁹ and Maeda *et al.*³⁵ These data are summarized in **Table 1**. Kurata³³ optimized the U–Pu–Zr ternary phase diagram on the basis of a thermodynamic assessment of elemental binary alloy systems U–Zr, U–Pu, and Pu–Zr. Ogata³⁶ expressed the solidus temperature T_{sol} (K) and liquidus temperature T_{liq} (K) obtained from the optimized ternary phase diagram by the following relations.

$$T_{\text{sol}} = A_0 + A_1 C_{\text{Zr}} + A_2 C_{\text{Zr}}^2 + A_3 C_{\text{Zr}}^3 \quad [1]$$

$$A_0 = 1408 - 1187C_{\text{Pu}} + 967C_{\text{Pu}}^2$$

$$A_1 = 572 - 732C_{\text{Pu}} + 4960C_{\text{Pu}}^2$$

$$A_2 = 740 + 3305C_{\text{Pu}} - 29182C_{\text{Pu}}^2$$

$$A_3 = -624 - 3139C_{\text{Pu}} + 36120C_{\text{Pu}}^2$$

$$T_{\text{liq}} = B_0 + B_1 C_{\text{Zr}} + B_2 C_{\text{Zr}}^2 + B_3 C_{\text{Zr}}^3 \quad [2]$$

$$B_0 = 1408 - 749C_{\text{Pu}} + 93C_{\text{Pu}}^2$$

$$B_1 = 1313 + 3869C_{\text{Pu}} + 5072C_{\text{Pu}}^2$$

$$B_2 = -1052 - 6637C_{\text{Pu}} - 44769C_{\text{Pu}}^2$$

$$B_3 = 521 + 1683C_{\text{Pu}} + 66380C_{\text{Pu}}^2$$

Here, C_{Zr} , C_{Pu} , and C_{U} are the atomic fractions of Zr, Pu, and U, respectively. Correlations [1] and [2] are applicable for $C_{\text{Pu}}/C_{\text{U}} < 1$ and $C_{\text{Zr}} < 0.8$. In the case of the U–Zr binary alloy, $C_{\text{Pu}} = 0$. The values calculated by using these relations are shown in **Figure 3** and also

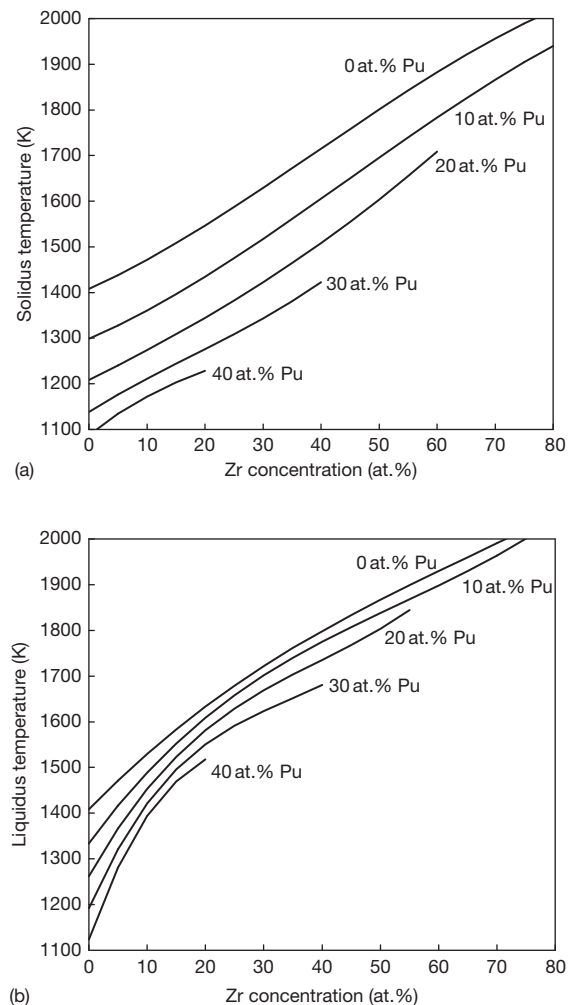


Figure 3 Evaluated solidus and liquidus temperatures of U–Zr and U–Pu–Zr alloys.

in [Table 1](#), which indicate that there are deviations from the reported data: <60 K for the solidus and <130 K for the liquidus.

3.01.2.1.3 Phase transition temperatures

A U–Zr binary phase diagram was shown by Massalski.³⁷ Kurata *et al.*³³ evaluated this alloy system on the basis of various published thermochemical data and phase boundary data. O’Boyle *et al.*²⁵ experimentally determined the U–Pu–Zr ternary phase diagram at several temperature cross sections. Kurata³³ optimized the U–Pu–Zr ternary phase diagram, as discussed in [Section 3.01.2.1.2](#). [Figure 4](#) illustrates the phase transition temperatures estimated from several U–Pu–Zr isotherms by O’Boyle *et al.*²⁵ The phases shown in the figure are as follows²⁵:

- γ : Body-centered cubic (bcc) allotropic modification of uranium that has complete solid solubility

for bcc ε -plutonium and bcc β -zirconium; γ_1 and γ_2 are the uranium-rich and zirconium-rich modifications of γ , respectively, that are formed by a monotectoid reaction in the U–Zr binary system.

- α : Orthorhombic allotropic modification of uranium that dissolves up to 15 at.% of plutonium, but has limited solubility for zirconium.
- β : Tetragonal allotropic modification of uranium that dissolves up to 20 at.% of plutonium, but has limited solubility for zirconium.
- η : A high-temperature intermediate phase in the U–Pu binary system that is believed to be tetragonal and has limited solubility for zirconium.
- ζ : A complex cubic U–Pu intermediate phase that dissolves up to 5 at.% zirconium.
- δ : A hexagonal intermediate phase in the U–Zr system that occurs approximately at the composition UZr_2 and has extensive solid solubility for plutonium.

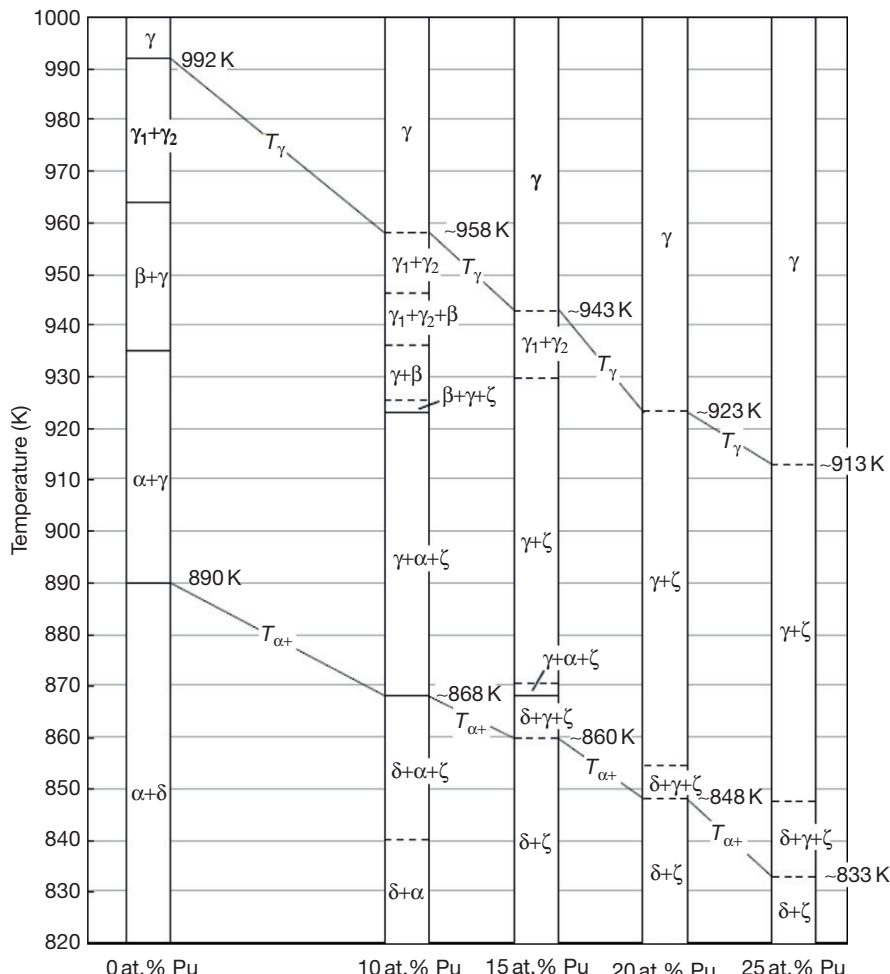


Figure 4 Phase transition temperatures of U–Zr and U–Pu–Zr alloys estimated from O’Boyle and Dwight.²⁵

In **Figure 4**, T_α is the temperature below which the γ -phase disappears, and T_γ is the temperature above which the γ solid solution dominates.

3.01.2.1.4 Heat capacity

Heat capacity data for U–Pu–Zr alloys have not been reported to date. Takahashi *et al.*³⁰ and Matsui *et al.*³¹ measured the heat capacities of U–Zr alloys, which are presented in **Figure 5**. The curves in the figure are the heat capacities that have been calculated on the basis of a thermodynamic assessment of the U–Zr binary system by Kurata *et al.*³² The calculated values below 850 K are in good agreement with the data by Matsui *et al.*,³¹ but the calculated values above 900 K are in good agreement with the data by Takahashi *et al.*³⁰ Because the heat capacity of plutonium is similar to that of uranium, the heat capacity of U–Pu– x Zr alloys may be similar to that of U– x Zr alloys.

3.01.2.1.5 Thermal conductivity

Touloukian *et al.*²⁴ contains the thermal conductivity data on U–Zr alloys, which can also be found in Rough.¹⁸ The data for U–25.1 at % Zr alloy

was measured by a comparative method at ANL.²⁷ Takahashi *et al.*²⁸ measured the U–Zr thermal diffusivities by a laser-flash method, from which they evaluated the thermal conductivities based on the U–Zr heat capacities estimated from the elemental heat capacities. These data are summarized in **Figure 6**. Matsui *et al.*³¹ evaluated the thermal conductivities of the U–20 at.% Zr alloy on the basis of its heat capacity that they measured by the direct heating pulse calorimetry as well as the U–Zr thermal diffusivities measured by Takahashi *et al.*²⁸ The evaluated values were consistent with the data reported in Touloukian *et al.*,²⁴ Argonne National Laboratory report,²⁷ and Takahashi *et al.*²⁸ The data for U–Pu–Zr alloys, which were measured by a comparative method with reference to an Armco iron sample, are contained in an Argonne National Laboratory report.²¹ These data are listed in **Figure 7**, with the U–Pu data reported in Kelman *et al.*²²

Billone *et al.*³⁸ showed the thermal conductivity relation for U–Zr and U–Pu–Zr alloys as follows:

$$k_0 = A + BT + CT^2 \quad [3]$$

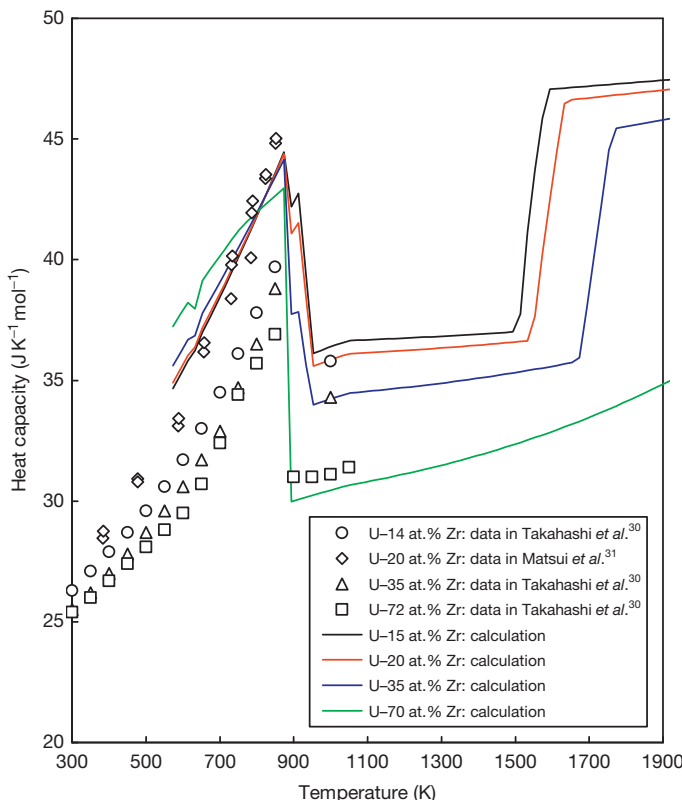


Figure 5 Heat capacity of U–Zr alloys. ‘Calculations’ are based on Kurata *et al.*³²

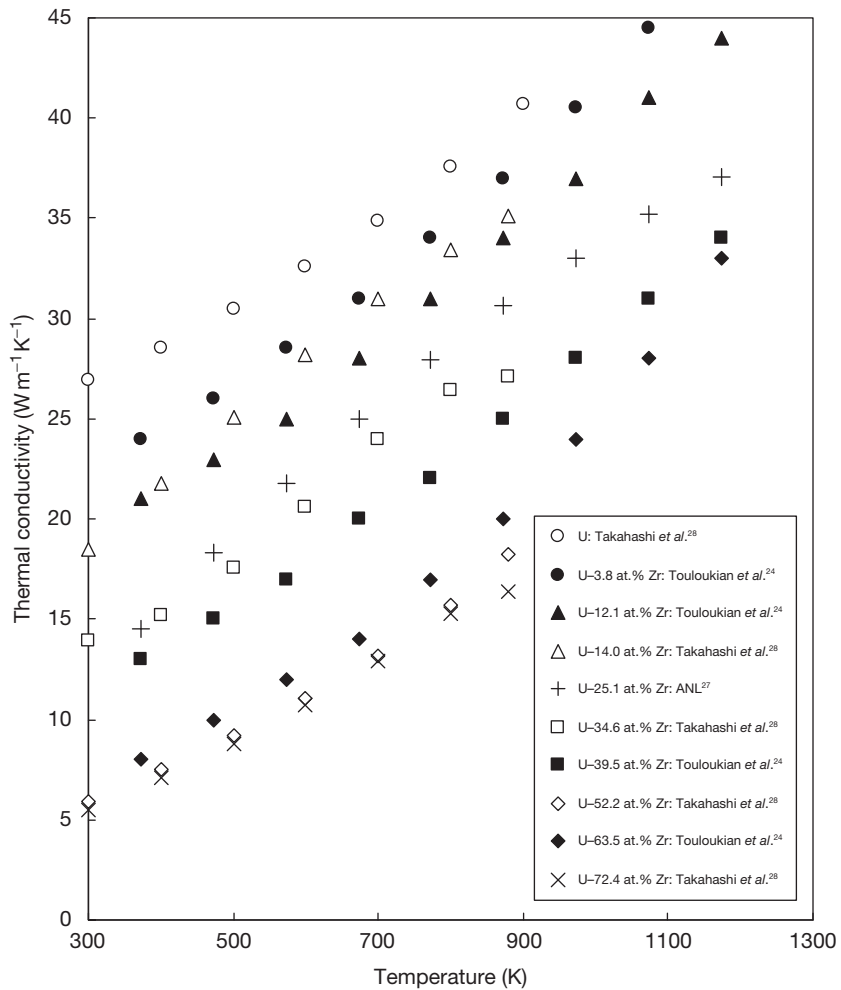


Figure 6 Thermal conductivity data of U–Zr alloys.

$$A = 17.5 \times \left(\frac{1 - 2.23W_Z}{1 + 1.61W_Z} - 2.62W_P \right)$$

$$B = 1.54 \times 10^{-2} \times \left(\frac{1 + 0.061W_Z}{1 + 1.61W_Z} - 0.90W_P \right)$$

$$C = 9.38 \times 10^{-6} \times (1 - 2.70W_P)$$

where k_0 is the thermal conductivity ($\text{W m}^{-1} \text{K}^{-1}$), T is the temperature (K), and W_Z and W_P are the weight fractions of the zirconium and plutonium, respectively.

Relation [3] does not reflect the U–Zr data by Takahashi *et al.*,²⁸ which came after the publication of Billone *et al.*³⁸ Ogata³⁶ proposed the following simpler relation for the U–Zr and U–Pu–Zr thermal conductivities, reflecting all of the available data plotted in Figures 6 and 7.

$$\begin{aligned} k_0 = & 16.309 + 0.02713T + 46.279C_{\text{Zr}} \\ & + 22.985C_{\text{Zr}}^2 - 53.545C_{\text{Pu}} \end{aligned} \quad [4]$$

$$T < 1173\text{K}, C_{\text{Zr}} < 0.72, C_{\text{Pu}} < 0.16$$

where C_{Zr} and C_{Pu} are the atomic fractions of Zr and Pu, respectively. For the U–Zr binary alloy, $C_{\text{Pu}} = 0$. The values calculated for U–Pu–22 at.% Zr alloys with relation [4] are shown in Figure 8.

3.01.2.1.6 Thermal expansion

The thermal expansion of U–Zr alloys is reported in Rough,¹⁸ but these data are for the Zr-rich side. For U–Pu–Zr alloys, the data are contained in Boucher and Barthelemy¹⁹ and Kelman *et al.*,²² as summarized in Table 2.

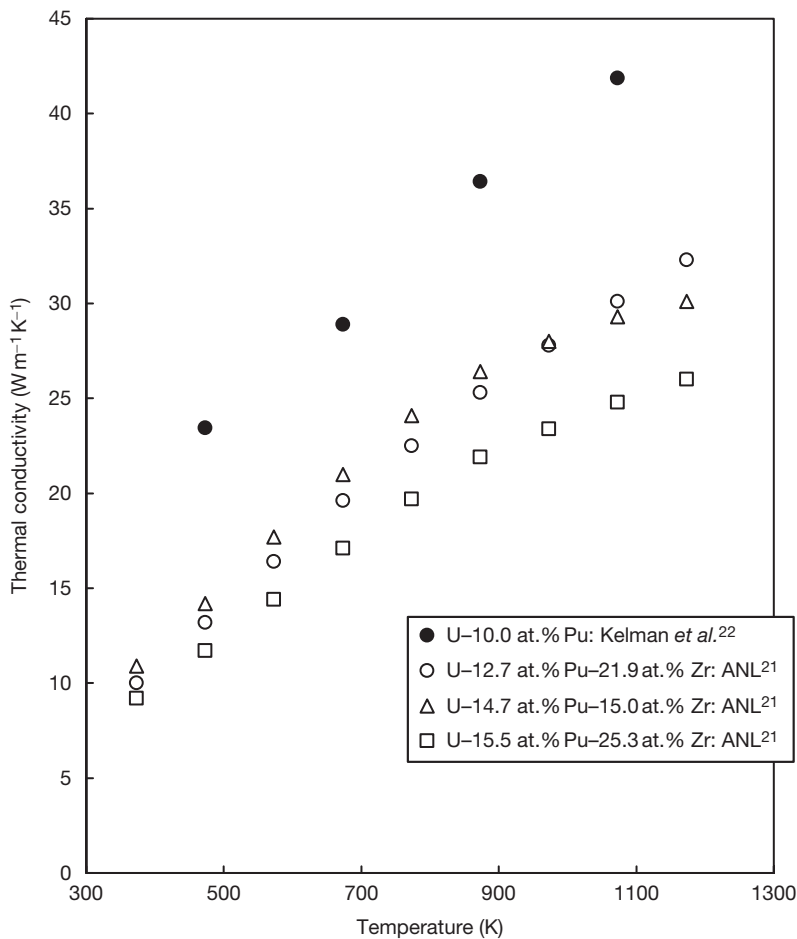


Figure 7 Thermal conductivity data of U-Pu-Zr alloys.

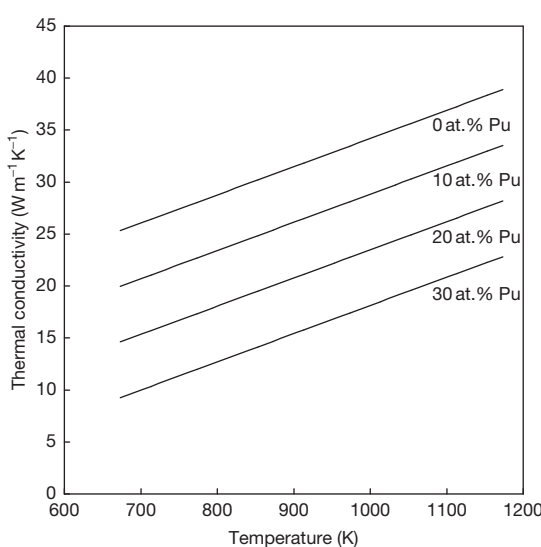


Figure 8 Thermal conductivity of U-Zr and U-Pu-Zr alloys. Evaluated by eqn [4].

3.01.2.2 Mechanical Properties

The modulus of elasticity, yield strength, and ultimate tensile strength of various compositions of U-Pu-Zr alloys are given by Harbur *et al.*²³ and Kittel *et al.*,²⁶ and summarized in [Table 3](#) and [Figures 9–11](#). These mechanical property data do not show obvious dependency on the alloy composition, but suggest a decreasing trend with increasing temperature. The considerable variation in the data may be attributed to differences in sample preparation methods such as heat treatment. Rough¹⁸ has reported the modulus of elasticity data for U-Zr alloys, which are shown in [Table 3](#) and [Figure 9](#). The figure shows that U-Zr alloys have a higher modulus of elasticity than U-Pu-Zr alloys, which decreases with increasing temperature. Kurata *et al.*³⁹ measured the modulus of elasticity and Poisson's ratio for U-19Pu-10Zr and U-19Pu-10Zr-5MA-5RE (in wt%), where RE is an abbreviation for a mixture of lanthanide elements, at

Table 2 Thermal expansion data of U–Pu–Zr alloys

<i>Ref.</i>	<i>Composition (at.%)</i>	<i>Temperature range (K)</i>		<i>Thermal expansion (K⁻¹)</i>
22	U–10Pu–15Zr	<861	868–953	953–1223
		18.3×10^{-6}	6.0×10^{-5}	18.1×10^{-6}
	U–12.9Pu–22.5Zr	<868	868–938	938–1223
19		17.6×10^{-6}	7.4×10^{-5}	20.1×10^{-6}
	U–15Pu–30Zr	<868	868–933	933–1223
		17.5×10^{-6}	7.7×10^{-5}	20.0×10^{-6}
19	U–12.9Pu–22.5Zr	<873		
		$16.3 \pm 0.4 \times 10^{-6}$		
19	U–17.2Pu–22.5Zr	<859		
		$17.3 \pm 0.4 \times 10^{-6}$		

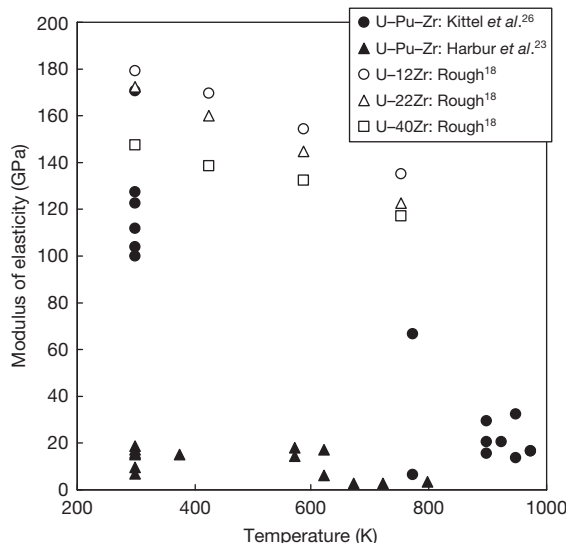
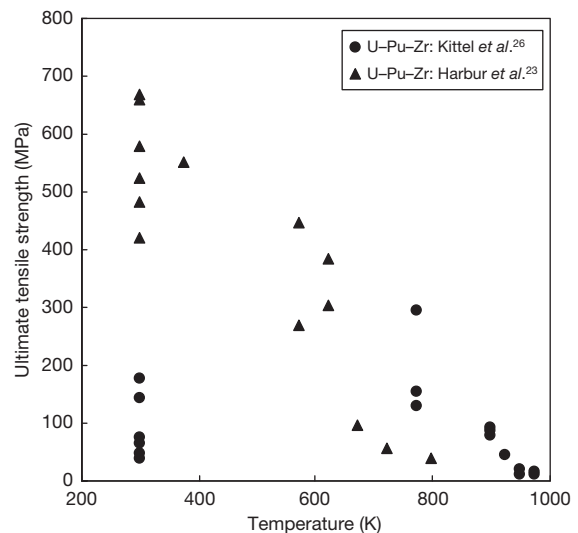
Table 3 Modulus of elasticity, yield strength, and ultimate tensile strength of U–Zr and U–Pu–Zr alloys

<i>Ref.</i>	<i>Composition (at.%)</i>	<i>Temperature (K)</i>	<i>Modulus of elasticity (GPa)</i>	<i>Ultimate tensile strength (MPa)</i>	<i>Yield strength, 2% offset (MPa)</i>
26	U–10.0Pu–14.9Zr	298	171	178	
		773	67	295	
		898	29	93	85
		948	14	12	11
	U–10.0Pu–30.0Zr	298	100	48	
	U–15.0Pu–14.9Zr	298	104	39	
		773		155	
		898	21	87	40
		973	17	12	16
	U–15.0Pu–30.0Zr	298	127	76	
23		298	112	144	
		923	21	45	40
		973	17	17	16
	U–12.9Pu–22.5Zr	298	123	66	
		773	6	130	
		898	16	79	71
		948	32	21	17
	U–12.9Pu–22.5Zr	298	15	483	
		573	14	269	
		623	6	303	303
18		673	3	97	69
	U–11.7Pu–25.7Zr	298	16	524	
		373	15	552	
	U–12.4Pu–27.2Zr	298	19	660	
		573	18	447	
		623	17	384	379
		723	3	56	
		798	3	40	28
	U–12.3Pu–2.09Zr	298	7	579	
	U–13.6Pu–14.3Zr	298	17	669	
18	U–12.5Pu–26.6Zr	298	10	421	
	(arc-melted) U–6Zr	298	190		
		423	175		
		588	157		
		753	135		
18	U–12Zr	298	180		
		423	167		
		588	152		
		753	133		

Continued

Table 3 Continued

Ref.	Composition (at.%)	Temperature (K)	Modulus of elasticity (GPa)	Ultimate tensile strength (MPa)	Yield strength, 2% offset (MPa)
18	U-22Zr	298	164		
		423	155		
		588	143		
		753	125		
	U-40Zr	298	157		
		423	148		
		588	132		
		753	114		
18	(induction-melted)	298	179		
		423	170		
		588	154		
		753	135		
	U-22Zr	298	172		
		423	160		
		588	145		
		753	123		
	U-40Zr	298	148		
		423	139		
		588	132		
		753	117		

**Figure 9** Modulus of elasticity of U-Zr and U-Pu-Zr alloys.**Figure 10** Ultimate tensile strength of U-Pu-Zr alloys.

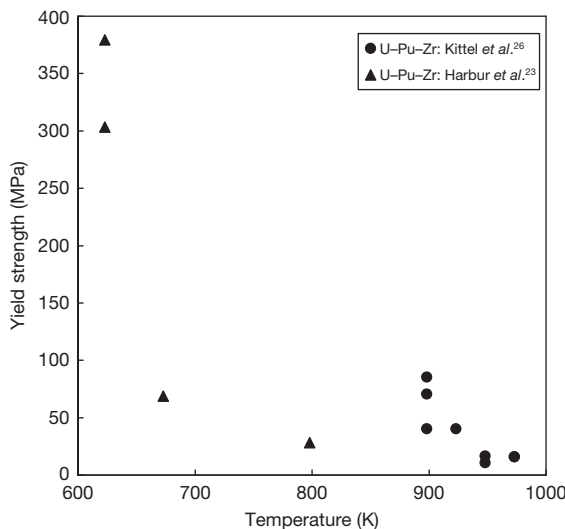
room temperature by an ultrasonic method. The measured data are shown in **Table 4**.

The times to attain 2% creep strain in U-Pu-Zr alloys are listed in Kelman *et al.*,²² Harbur *et al.*,²³ and Kittel *et al.*²⁶ The data in Harbur *et al.*²³ are for the temperature range of 563–773 K, and in Kelman *et al.*²² and Kittel *et al.*²⁶ from 873 to 973 K. **Table 5** summarizes the creep strain rates calculated from

these time data. On the other hand, the following relations for the steady-state creep strain rate of U-Pu-Zr alloys are given in Gruber and Kramer.⁴⁰ In the low-temperature regime, where creep is dominated by the deformation of the α -uranium matrix

$$\dot{\varepsilon} = (0.5 \times 10^4 \bar{\sigma} + 6.0 \bar{\sigma}^{4.5}) \exp(-26170/T) \quad [5]$$

and at higher temperatures where the γ solid solution phase is formed,

**Figure 11** Yield strength of U-Pu-Zr alloys.**Table 4** Mechanical properties of U-Pu-Zr and U-Pu-Zr-MA-RE alloys

Composition (at.%)	U-19Pu-10Zr	U-19Pu-10Zr 5MA-5RE*
Density (g cm^{-3})	15.501	14.510
Elastic modulus (GPa)	93.306	85.215
Shear modulus (GPa)	35.391	32.647
Poisson ratio	0.317	0.305

*MA: Mixture of Np and Am; RE: Mixture of Np, Ce, and Y

$$\dot{\varepsilon} = (8.0 \times 10^{-2} \bar{\sigma}^3) \exp(-14350/T) \quad [6]$$

where $\dot{\varepsilon}$ is the creep strain rate (s^{-1}), $\bar{\sigma}$ is the stress (MPa), and T is the temperature (K). Relation [6] for the γ solid solution is consistent with the data in Kelman *et al.*²² and Kittel *et al.*,²⁶ but eqn [5] gives the lower bound of the data in Harbur *et al.*²³ For U-Zr alloys, some data for the Zr-rich side appear in Rough.¹⁸

Ogata *et al.*⁴¹ estimated the creep strain rate of U-22.5 at.% Zr alloy from the relaxation behavior of compressive stress applied to the sample above 1000 K. These data suggest that the creep strain rate of U-Zr alloys is significantly lower than that of U-Pu-Zr alloys. Robinson *et al.* have reported the creep strain rate data for uranium metal.⁴²

3.01.2.3 Diffusion Properties

The migration (or diffusion) of fuel constituents and fission products occurs in U-Zr and U-Pu-Zr fuel pins during neutron irradiation, as described in **Section 3.01.4**. The mechanisms of formation, migration, and growth of fission gas bubbles are related to the diffusion process of the fission gas atoms and fuel constituents in the fuel alloys, as discussed in **Chapter 3.23, Metal Fuel Performance Modeling and Simulation**. The diffusion properties are important in understanding and modeling the metal fuel irradiation behavior.

Table 5 Creep strain rate of U-Pu-Zr alloys

Ref.	Composition (at.%)	Temperature (K)	Stress (MPa)	Creep strain rate (s^{-1})
26	U-10.0Pu-14.9Zr	898	39.2	6.7E-05
			4.9	2.2E-05
			9.8	6.7E-05
		948	19.6	1.1E-04
			39.2	3.3E-04
	U-15.0Pu-14.9Zr	898	9.8	6.7E-08
			19.6	1.6E-06
		948	39.2	3.3E-05
			4.9	3.3E-05
			9.8	3.3E-04
26	U-12.9Pu-22.5Zr	898	9.8	6.7E-08
			19.6	1.6E-06
		923	39.2	3.3E-05
			4.9	6.7E-08
			9.8	4.2E-06
	U-15.0Pu-30.0Zr	873	19.6	3.3E-04
			4.9	3.3E-09
			9.8	3.3E-08
		39.2	19.6	4.2E-07
			39.2	4.8E-06

Continued

Table 5 Continued

Ref.	Composition (at. %)	Temperature (K)	Stress (MPa)	Creep strain rate (s^{-1})
22	U-15.0Pu-30.0Zr	923	4.9	6.7E-08
			9.8	4.2E-06
			19.6	1.7E-04
		948	4.9	5.6E-06
			9.8	3.3E-05
			19.6	1.7E-04
		973	4.9	6.1E-06
			9.8	3.3E-05
			19.6	1.1E-04
		873	4.1	4.4E-09
			5.5	4.5E-09
			2.7	1.8E-06
23	U-12.9Pu-22.5Zr	948	4.1	6.2E-06
			5.5	1.3E-05
			2.7	2.4E-06
		973	4.1	5.2E-06
			5.5	1.4E-05
		623	137.8	1.1E-06
			206.7	1.7E-05
			275.6	3.7E-05
		673	55.1	1.1E-05
			68.9	3.7E-05
			75.8	1.1E-04
23	U-12.4Pu-27.2Zr	773	13.8	1.7E-05
			20.7	6.7E-05
			103.3	2.2E-05
		673	117.1	4.2E-05
			130.9	8.3E-05
			13.8	4.2E-05
		773	20.7	8.3E-05
			34.4	1.1E-05
		563	41.3	3.7E-05
			6.9	1.1E-03
			773	

Interdiffusion (chemical) diffusion coefficients in the bcc solid solution (γ -phase) of U-Zr binary alloys were measured by Adda *et al.*⁴³ in the temperature range 1223–1348 K. Ogata *et al.*⁴⁴ measured the diffusion coefficients in the γ -phase from 973 to 1223 K and found a depression in the coefficients at a zirconium content of about 0.3 atom fraction, corresponding to the miscibility gap at this zirconium content at 995 K. For the δ -phase, Akabori *et al.*⁴⁵ measured the interdiffusion coefficients at 823 and 853 K, and pointed out that the diffusion coefficients in the δ -phase are significantly smaller than those extrapolated from the γ -phase to the δ -phase. These U-Zr interdiffusion coefficients in the bcc solid solutions and the δ -phase are plotted in Figure 12. Adda *et al.*⁴⁶ evaluated the intrinsic diffusion coefficients of U and Zr in the γ -phase at 1223, 1273, and 1313 K, and showed that the U diffusion is much higher than the Zr diffusion in the U-rich side. The interdiffusion in U-Pu binary alloys at 1023 K was investigated by Petri *et al.*⁴⁷

For U-Pu-Zr ternary alloys, Petri and Dayananda⁴⁸ examined the interdiffusion coefficients at 1023 K, where the γ -phase is dominant, by using various diffusion couples consisting two alloys out of U, U-20Zr, U-22Pu-3Zr, and U-22Pu-20Zr (in at.%) alloys.

Thermodiffusion tests with U-Pu-Zr ternary alloys were performed by Harbur *et al.*,²³ Kurata *et al.*,⁴⁹ and Sohn *et al.*,⁵⁰ where the redistributions of U and Zr were observed. Analyses of these experimental data will contribute to an understanding of the phenomenon of fuel constituent migration in metal fuel.

3.01.2.4 Effects of MA Addition

The recent interest in MA transmutation, as discussed in Section 3.01.1, has led to the evaluation of the properties of MA-bearing fuel alloys. Kurata *et al.*³⁹ performed the dilatometric analysis of U-19Pu-10Zr, U-19Pu-10Zr-2MA-2RE, and U-19Pu-10Zr-5MA-5RE (in wt%) rod samples. Dilatometry

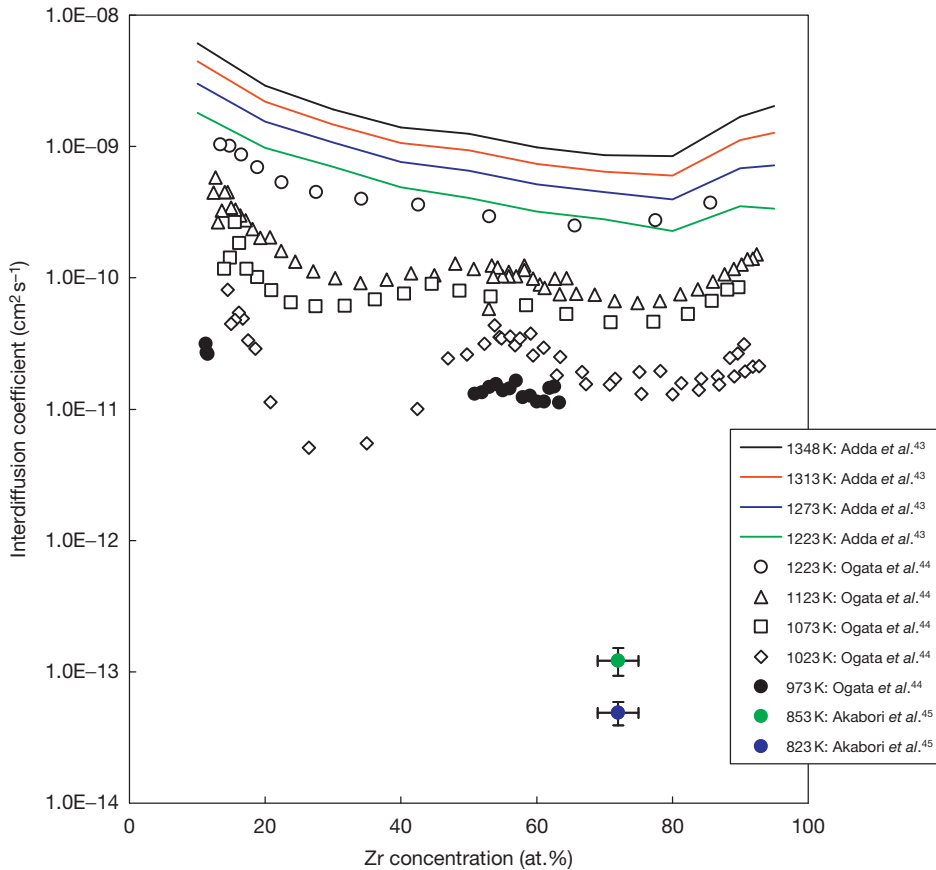


Figure 12 U-Zr interdiffusion coefficients in the bcc solid solutions and the δ -phase.

results indicated that there was no significant change at the phase transition temperature. The thermal conductivities of U-19Pu-10Zr and U-19Pu-10Zr-5MA-5RE (in wt%) were measured by a comparative method,³⁹ as shown in Figure 13. The figure suggests that the thermal conductivity of the U-Pu-Zr alloys is not sensitive to MA and RE additions up to 5 wt%. The elastic modulus, shear modulus, and Poisson's ratio of the U-19Pu-10Zr-5MA-5RE alloys were similar to those of the U-19Pu-10Zr alloy within experimental error,³⁹ as indicated in Table 4. Other property data for MA-bearing fuel alloys are now being measured at INL.

3.01.3 Metal Fuel Fabrication

A practical process for nuclear fuel fabrication needs to be cost efficient (or simple), suitable for remote operation, and capable of mass production while reducing the amount of radioactive waste. Injection casting is one of the processes that meets these needs

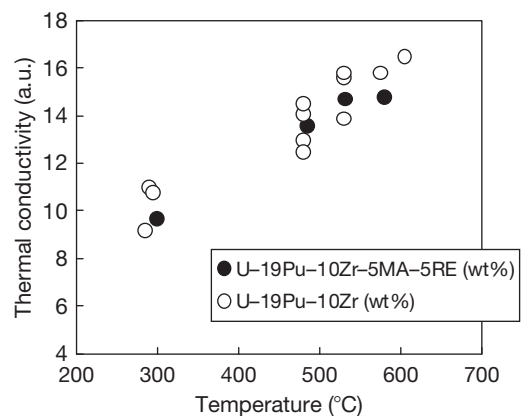


Figure 13 Measured thermal conductivities of U-19Pu-10Zr and U-19Pu-10Zr-3Np-2Am-0.2Y-1.2Ce-3.6Nd alloys.

and has been applied to fuel slug fabrication for the EBR-II driver and test fuel pins since the 1960s.^{1,51} In the demonstration of metal fuel recycle at ANL in the 1960s, the fuel slugs were refabricated remotely in the hot cell from partially decontaminated

radioactive uranium recovered from irradiated U–5 wt% Fs fuel.¹ The U–Zr and U–Pu–Zr fuel slugs for test subassemblies irradiated in EBR-II and FFTF were also fabricated by injection casting.⁵¹ More than 100 000 metal fuel pins including both U–5 wt% Fs and U–10 wt% Zr fuels were fabricated by injection casting in the United States.⁵¹ The metal fuel for earlier fast reactors, EBR-I and the Enrico Fermi Reactor, were made by various methods such as rolling and swaging, coextrusion, and centrifugal casting,² but these were not better than injection casting.

This section describes fuel slug fabrication methods, focusing on the injection casting process. The process of metal fuel pin assembly is also described. The development history and recent activities of metal fuel fabrication are summarized in Burkes *et al.*,^{51,52} which is referred to in many parts of this section.

3.01.3.1 Fuel Slug Fabrication

3.01.3.1.1 Injection casting

An outline of an injection casting process is illustrated in Figure 14, based on Burkes *et al.*,⁵¹ the Argonne National Laboratory,⁵³ and Ogata and Tsukada.⁵⁴ The starting materials, that is, uranium and zirconium metals (and uranium–plutonium alloy, when U–Pu–Zr casting), are charged into the graphite crucible in the injection casting furnace, and silica

tube molds with the top ends closed are set above the crucible. The crucible's interior is coated with yttria and the mold's interior is coated by zirconia for protection against reaction with molten uranium alloy. The furnace is closed and filled with highly purified Ar gas. The crucible is inductively heated up to ~1833 K, which is sufficiently higher than the liquidus temperature of the fuel alloy (e.g., 1656 K for U–10 wt% Zr). In order to ensure the homogeneity of the melt, it is kept at the high temperature and stirred electromagnetically by applying full power to the crucible.^{51,53,54} After the vessel is evacuated, the molds are lowered and their bottom ends are immersed in the melt. On again refilling the furnace with Ar gas, the pressure difference between the mold's interior (vacuum) and the furnace (Ar pressure) injects the melt into the molds. The injected melt is quickly solidified from the top to the bottom. After cooling, the fuel alloy castings are taken out of the molds. The mold must be broken when the casting is taken out. Therefore, the mold is not reusable, and the mold shards will be radioactive waste. However, the shards can be used as glass materials for waste forms such as glass-bonded sodalite, so that these may not be considered as additional waste.⁵⁵ The fuel slugs are obtained by shearing off both ends of the castings. It is unnecessary to grind the fuel slug surface unlike ceramic fuel pellets; the fuel slug

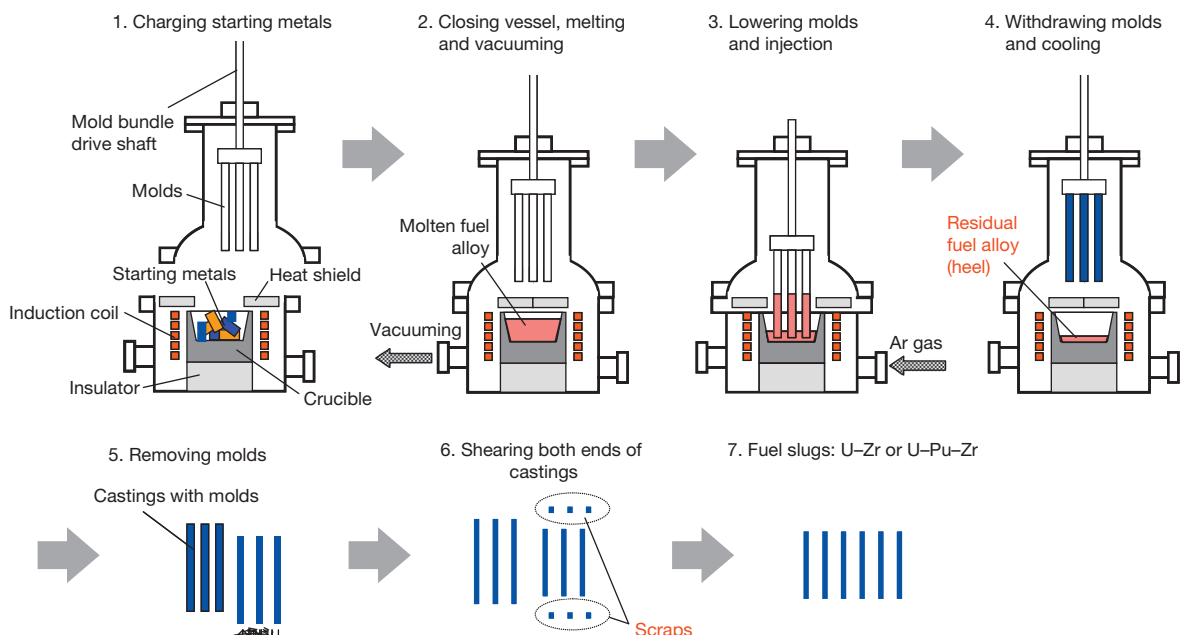


Figure 14 Outline of the injection casting process.

diameter is controlled by the inner diameter of the mold. The casting parameters such as molten alloy temperature, mold preheat temperature, pressurization rate in injection, and cooling rate after injection should be carefully determined according to the mold dimensions and fuel alloy composition. Inappropriate parameters may cause casting defects such as shrinkage pipes, microshrinkage, and hot tears.⁵¹

Injection casting tests with the furnace shown in Figure 15 were conducted by CRIEPI,⁵⁴ based on the experience in the United States. The maximum metal charge of the furnace is ~ 20 kg of the U–10 wt% Zr alloy per batch, which is close to that of commercial-scale equipment. The silica molds were 6 mm in inner diameter and 500 mm in length. The graphite crucible is inductively heated at a frequency of 3 kHz and a maximum power of 30 kW. The starting metals were basically uranium metal blocks and zirconium metal cut wire. In most of the casting batches, slugs, heels, and scraps from the preceding casting batch were also charged, simulating a practical fuel slug casting process. These metals were weighed and adjusted so that the composition of the alloy was U–10 wt% Zr. Complete melting and dissolution of the metals were ensured by maintaining the metal temperature at 1780–1840 K for about 30 min. The argon gas pressurization rate in injection was 0.2 MPa s^{-1} and the terminal pressure was 0.2 MPa. Both ends of the castings were cut off using a shearing device, and 400-mm-long U–Zr slugs were obtained. Ten casting test batches resulted in the production of more than ~ 500 slugs of U–10 wt% Zr alloy. The quality of the produced

U–Zr slugs was satisfactory with respect to the provisional specifications: average diameter precision ± 0.05 mm; local diameter precision ± 0.1 mm; density $15.3\text{--}16.1 \text{ g cm}^{-3}$; zirconium content 10 ± 1 wt%; the total amount of impurities (O, C, N, and Si) <2000 ppm. Typical distributions of the slug diameter and density are presented in Figure 16. Figure 17 shows the relationship between the slug average diameter and the mold inner diameter measured at the bottom-end opening. The solid line in the figure denotes the slug diameters calculated by subtracting the thermal shrinkage of the U–Zr alloy and the zirconia coating thickness (estimated to be 0.01 mm) from the mold inner diameter. In this calculation, it was assumed that the alloy was cooled from the solidus temperature of 1566 K for the U–10 wt% Zr alloy (see Section 3.01.2.1.2) down to room temperature, and the thermal expansion coefficient of the γ



Figure 15 Injection casting furnace for U–Zr casting tests.

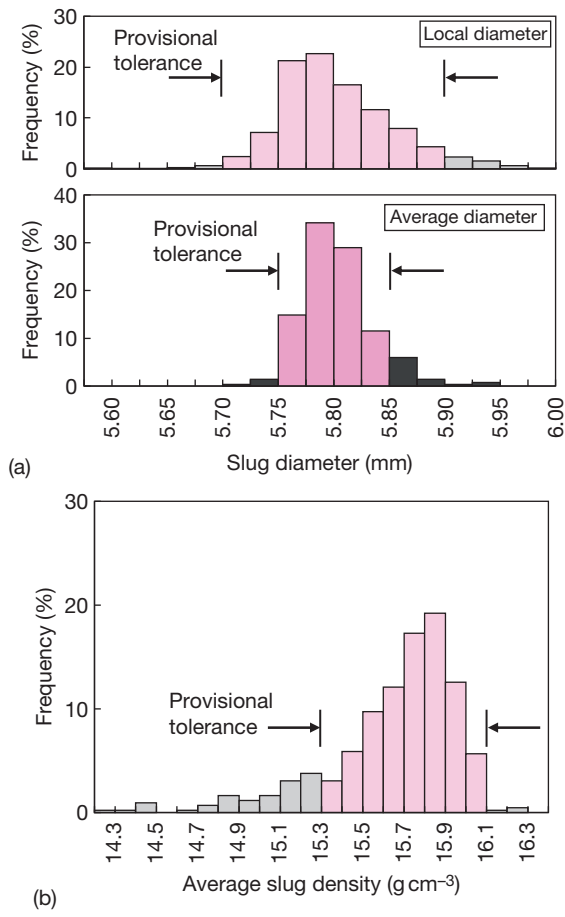


Figure 16 Distributions of diameter and density of the fabricated U–Zr alloy slugs (a) Local and average diameter and (b) density.

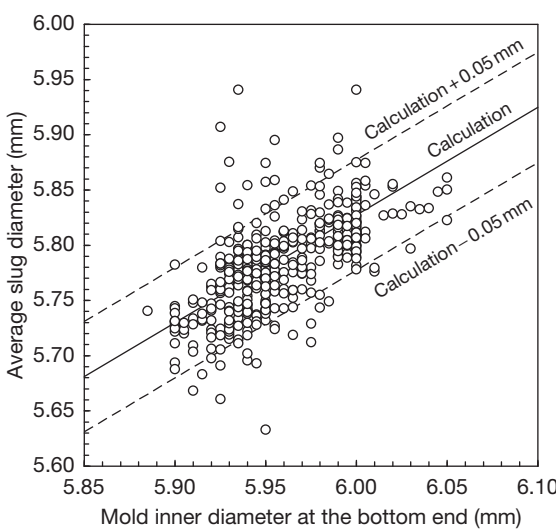


Figure 17 Relationship between the slug average diameter and the mold inner diameter measured at the bottom-end opening.

solid solution of the U–Zr alloy was approximated by that of the U–Pu–Zr alloy, that is, $2.0 \times 10^{-5} \text{ K}^{-1}$ (see Section 3.01.2.1.6). Figure 17 indicates that most of the average slug diameters fall within the range of $\pm 0.05 \text{ mm}$ of the calculated value, so that the slug diameter can be controlled by the mold inner diameter. Despite the repeated use of heel and scrap, the total amount of impurities (O, C, N, and Si) was still lower than the provisional limit. In the last test batch, 1.1Mo, 0.8Pd, 0.06Ce, and 0.1Nd (in wt%) were added to the metal charge, simulating the fission product elements that may remain in the pyroprocess products. Precipitations of these elements were not detected in the U–Zr slugs. Improvement in throughput can be achieved by increasing the casting ratio (weight percentage of the injected metal relative to the charged metal). Optimizing the depth of the mold bottom end in the molten fuel and the array pattern of the mold bundle resulted in a reasonable casting ratio of 70–80%.

The influence of some of the casting parameters, for example, molten alloy temperature, mold preheat temperature, and pressurization rate in injection, on the maximum casting length can be predicted by calculating the temperature of the molten fuel alloy during injection casting. For this purpose, an injection-casting simulation code, ICAST, was developed.⁵⁶ The ICAST code calculates the temperature of the mold and fuel alloy during each step of the injection casting process: mold preheating, injection, and cooling. Radiation heat transfer from the molten alloy surface and crucible wall is essential for

predicting the mold temperature in the mold preheating step. The gap conductance between the mold and molten fuel alloy also has a significant influence on the fuel alloy temperature calculation in the injection step. The calculation by ICAST showed that the coating inside the mold acts as a thermal insulator for the molten alloy to be injected higher. This was verified by an injection-casting test without the mold coating.

KAERI has experience in injection casting of U–10 wt% Zr–(2,4,6) wt% Ce ternary alloys,⁵⁷ where Ce was a surrogate element for MA or rare earth fission products. The test result showed that Ce particles were dispersed in the U–Zr matrix.

Recent interest in MA-bearing fuel has resulted in a reevaluation of injection casting. A major problematic point in the injection casting of MA-bearing metal fuel slugs is that the crucible used in injection casting is not a closed system, where a relatively high vapor pressure of Am raises concerns about contamination of the furnace's interior and loss of Am from the process. Three full-length fuel slugs ($4.3 \times 340 \text{ mm}$) of the U–20Pu–10Zr–1.2Am–1.3Np (in wt%) alloy were fabricated by injection casting for the X501 irradiation test.^{58–61} Although no unusual macrosegregation of the major constituents was observed, only 60% of the initial Am charge was present in the as-cast fuel. Am loss was attributed to volatile impurities (Ca and Mg) in the Am–Pu feed stock⁶¹ and evaporation at the casting temperature, 1465 °C. Chemical analysis of sections from the top, center, and bottom of the fuel slug revealed that the U, Pu, Zr, and Np levels were axially uniform, within experimental error, while the Am level was low (1.03 wt%) in the bottom section compared to those in the top and central sections (1.33 and 1.32 wt%, respectively).⁵⁹ Trybus⁶² performed an injection-casting test with U–7.5 wt% Zr–1.5 wt% Mn alloy, which was the surrogate alloy for U–Pu–Zr–Am–Np alloys. Mn has a vapor pressure similar to that of Am at the casting temperature. In the surrogate casting test, the alloying temperature and the vacuum just before injection were reduced to 1455 °C and $\sim 13.3 \text{ kPa}$, respectively, from those in the X501 fuel casting, which were 1495 °C and $\sim 670 \text{ Pa}$, respectively. The casting was successfully completed, and chemical analysis of the samples from the slug center indicated 1.42 wt% Mn, which is 90% of the initial Mn charge. This means that minimal Mn (and Am) loss is possible by changing the casting parameters.⁶²

According to the comprehensive discussion on Am evaporation of Burkes *et al.*,⁵² the Am evaporation can be reduced by decreasing the fuel melt temperature,

increasing the cover gas pressure, and/or reducing the Am concentration gradient in the cover gas. The fuel melt temperature can be decreased by adjusting the fuel alloy composition, for example, by reducing the Zr content in the fuel alloy.⁶³ From the standpoint of increased cover gas pressure, injection casting may be disadvantageous because the furnace is evacuated before injection. The Am concentration gradient can be reduced by using a closed system for fuel alloy melting. This is possible for the methods presented below, other than injection casting.

Nakamura *et al.*⁶⁴ recently fabricated U–Pu–Zr metal fuel slugs by injection casting for an irradiation test in the experimental fast reactor, Joyo. In the fabrication process, a small amount of Am (~ 0.3 wt%) accompanied the fuel alloy. Chemical analysis and γ spectrometry of the samples from the graphite crucible and yttria coating indicated that Am selectively reacted with the graphite crucible and yttria coating. This suggests that attention needs to be paid not only to Am volatility but also to its chemical reactions with process materials.

3.01.3.1.2 Other methods

3.01.3.1.2.1 Centrifugal casting

In a centrifugal casting process, the molten fuel alloy is poured vertically onto a rotating plate (distributor), where the melt flow turns to the horizontal direction. The molds are aligned on the edge of the distributor and rotate with it. The melt is injected into the molds by the centrifugal force. This process was used to cast U–2 wt% Zr alloy fuel slugs for EBR-I, which were significantly larger in diameter than for EBR-II (9.8 mm compared to 3.3–4.4 mm).⁵²

Although centrifugal casting could potentially be used to fabricate fuel slugs with dimensions typical of those in a commercial fast reactor, the process has been considered somewhat complicated and time consuming.⁵² The number and type of manipulations required to assemble and disassemble the furnace and molds are significant, and there are concerns about the relatively low throughput, compared with other fabrication processes.⁵²

3.01.3.1.2.2 Continuous casting

Continuous casting is widely used in steel plants, and is also one of the candidates for MA-bearing metal fuel slugs. This process eliminates the need to use molds. KAERI produced a uranium rod with a uniform diameter of 13.7 mm and a length of 2.3 m.⁵⁷ The continuous casting of U–Zr alloy slugs with a smaller diameter is under way.

Optimizing the casting conditions is difficult when the fuel alloy has a large solidification range^{52,57} (temperature difference between the solidus and the liquidus). A wide solidification range can lead to microshrinkage effects and loss of process control during casting.⁵² Furthermore, pulling of the cast must be properly aligned to avoid any asymmetric variations in the rod diameter, thereby increasing the complexity of the unit for remote operation.⁵² Finally, if continuous casting were to be used, the process would need to be highly automated to minimize the extent of human interaction required for casting a significant number of fuel slugs.⁵²

3.01.3.1.2.3 Gravity casting

Renewed interest is being taken in gravity casting, where fuel melt is poured into molds by gravity with or without the assistance of a pressure difference. In gravity casting as well as centrifugal casting and continuous casting, the furnace containing the fuel melt is not evacuated, unlike in injection casting. This is favorable for suppressing Am evaporation. The gravity casting system is relatively simple.

Lee *et al.*⁵⁷ fabricated U–10 wt% Zr rods by gravity casting with a split graphite mold and a quartz tube mold. A two-piece graphite mold was also used to facilitate the demolding operation after the casting.⁵⁷ Vacuum-assisted gravity casting was also tested by KAERI, and U–10 wt% Zr and U–10 wt% Zr–6 wt% Ce alloys slugs were successfully fabricated.⁵⁷

An advanced casting system (ACS) is being developed at INL to demonstrate minimal actinide fuel loss by rapid melting and casting under careful atmosphere control in a reusable crucible and molds.⁶⁵ The first step of ACS development activity includes design and construction of a bench-scale casting system (BCS), sized for 50–300 g castings, for use with MA-bearing fuel alloys to demonstrate minimal transuranium element (TRU) loss.⁶⁵ BCS is based on bottom-poured casting assisted by a pressure differential, and has the capability to be configured for injection casting.⁶⁵

3.01.3.1.2.4 Atomizing

The concept of He-bond particulate metal fuel⁶³ was proposed as an advanced metal fuel, where a cladding tube is filled with fuel alloy particles and the spaces among the particles are filled with He gas, not sodium. A mixture of particles with two different diameters can attain a fuel smear density (filling fraction) of about 75%.⁶³ The He-bond particulate metal fuel has the following advantages: the He-bond

allows the gas plenum to be positioned below the fuel column section, so that the gas plenum temperature is reduced and the fuel pin length can be shortened; nonuse of bond sodium will save the corresponding amount of oxidizing agent required in the electrorefining process; and the fuel alloy particles can be fabricated by gas atomization or centrifugal atomization, neither of which needs molds and are expected to have higher production throughput than injection casting. Furthermore, the furnace for atomizing can be a closed system for fuel alloy melting, which is suitable for MA-bearing fuel fabrication.

Spherical uranium alloy particles such as those of U–Mo and U–Zr were successfully fabricated by centrifugal atomization.⁵⁷

3.01.3.2 Fuel Pin Assembly

A metal fuel pin assembling process is schematically shown in [Figure 18](#). This is based on the scheme used for the fabrication of the metal fuel test pins⁶⁶ to be irradiated in the experimental fast reactor, Joyo. This scheme is similar to that for EBR-II driver fuel pins.¹ Fuel slugs are checked for dimensions and weight (or density). Bond sodium is extruded by using a bond sodium extruder and shaped into rods. The weight of the bond sodium to be loaded into the cladding is determined from the measured or evaluated dimensions of the cladding's interior and the fuel slug so as to meet the gas plenum volume specification. The rod-shaped bond sodium is first inserted into the cladding tube with the lower-end plug welded, followed by the fuel slug(s). One or two more slugs are inserted as required. After welding the upper-end plug, the fuel pin is checked for leaks. Then, the fuel pin is heated up to $\sim 500^\circ\text{C}$ and oscillated vertically so that the annular gap between the cladding and fuel slug is filled with the bond sodium. The gas plenum length is checked by an X-ray transmission method.

The US historical experience of metal fuel pin assembling is described in detail in Burkes *et al.*⁵¹

3.01.4 Steady-State Irradiation Behavior

In the course of neutron irradiation, metal fuel exhibits a characteristic behavior, as shown in [Figure 19](#), which is different from that of ceramic fuel. For example, when compared with oxide fuel, a metal fuel slug tends to hold more fission gas atoms, and accordingly showing a higher rate of gas swelling in the early stages of irradiation; a higher creep rate of

the fuel alloy leads to high compressibility of the swollen fuel slug; and lanthanide fission products agglomerate at the peripheral region of the fuel slug and react with the Fe-based cladding. These phenomena are closely related to each other.

This section describes such characteristic steady-state irradiation behavior of metal fuel, after reviewing the irradiation tests of U–Zr and U–Pu–Zr fuel pins. Recent MA-bearing metal fuel tests and their limited data are also explained. A large part of this section is based on comprehensive documents on metal fuels.^{3–5,69–71}

3.01.4.1 Steady-State Irradiation Tests

The U–Pu–Zr alloys were first irradiation-tested in the CP-5 thermal reactor,⁶⁷ where six U–15 wt% Pu–12 wt% Zr slugs clad with 304SS, 316SS, and Hastelloy-X were irradiated at a maximum cladding temperature of 610°C up to 2.4 at.% burnup, and one U–18.5 wt% Pu–14.1 wt% Zr slug clad with V–20Ti at a maximum cladding temperature of 655°C up to 12.5 at %. The fuel slug length was scaled down by a factor of seven from that of the EBR-II driver, that is, 34.3 cm. Subsequently, 16 U–15 wt% Pu–10 wt% Zr (nominal composition) fuel slugs clad with 304LSS, 316SS, Hastelloy-X, and Hastelloy-X-280 were irradiated in EBR-II at a maximum cladding temperature ranging from 600 to 652°C up to about 4.5 at.% burnup without failure.⁶⁸ These early irradiation tests in the 1960s revealed the main features of irradiation phenomena such as fission gas release, restructuring, fuel constituent migration, and cladding wastage by lanthanide fission products.

The main body of metal fuel irradiation data was gained through irradiation tests conducted in the IFR program.⁶ Beginning with three lead test assemblies, ~ 600 U–Pu–Zr test pins and 8000 U–Zr test pins were irradiated in EBR-II and FFTF.⁸ In the tests, fuel pins with a wide variety of specifications were irradiated under a wide range of conditions, as follows:⁵ Pu contents 0–28 wt%; Zr content 2–14 wt%; smear density 70–85%; cladding material: an austenitic stainless steel (316SS), a titanium-stabilized austenitic stainless steel (D9), and a ferritic/martensitic steel (HT9); peak burnup ~ 19 at.%; and peak cladding temperature $< 660^\circ\text{C}$. The full lineup of test assemblies in the IFR program is summarized in Crawford *et al.*⁵ Representative test assemblies are listed in [Table 6](#).

Recent metal fuel irradiation tests have focused on MA-bearing metal fuel, as summarized in [Table 7](#).

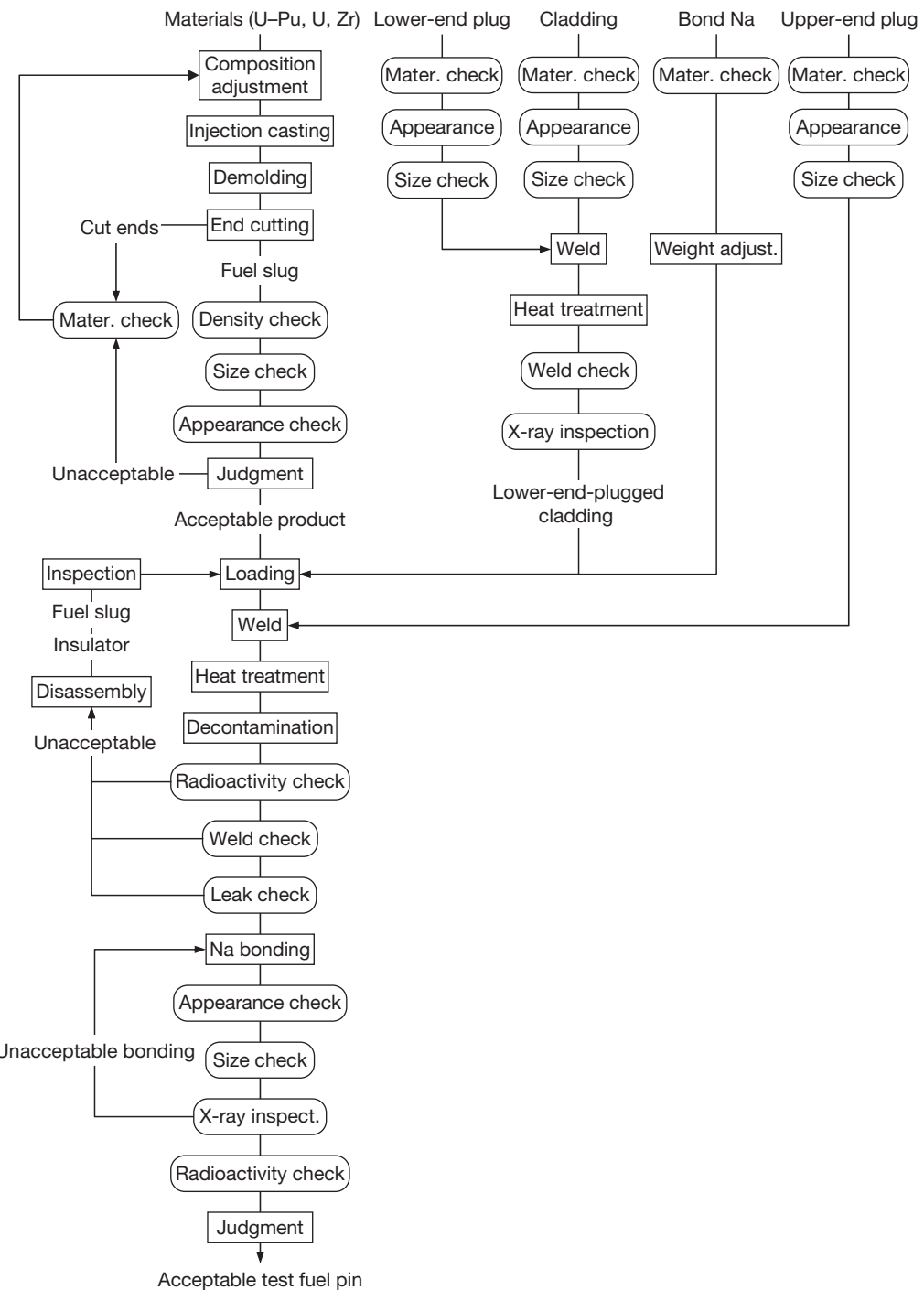


Figure 18 Metal fuel pin assembling process.

Among them, the X501^{58–60} test assembly has been completed, and postirradiation examinations for the METAPHIX,^{72–76} AFC-1,^{77–79} AFC-2,^{80,81} and FUTURIX-FTA^{82,83} tests are ready or in progress. Some of the test results have been reported.

3.01.4.2 Fuel Constituent Migration

The as-cast metal fuel slug shows macroscopically uniform distribution of the fuel constituents. Its initial microstructure consists essentially of a metastable

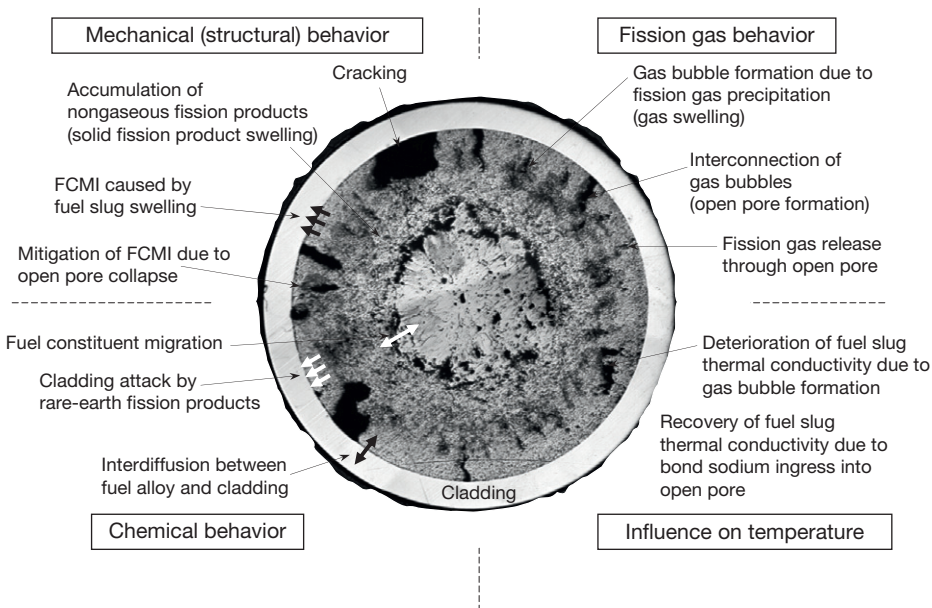


Figure 19 Outline of irradiation behavior of a metal fuel.

low-temperature α -phase supersaturated with Zr, according to Hofman *et al.*⁶⁷ In the course of irradiation, this phase will transform into phase structures stable at the temperatures of the respective regions of the slug (see Figure 4). Along with the phase transformation, the fuel constituents migrate radially.^{60,69,84,85} A typical example of fuel constituent migration is shown in Figure 20.⁸⁶ The chart superimposed on the figure shows the characteristic X-ray intensities from the constituents U, Pu, and Zr. According to Kim *et al.*,⁶⁰ Hofman *et al.*,⁶⁷ Porter *et al.*,⁸⁴ Hofman *et al.*,⁸⁵ and Kim *et al.*,⁸⁶ the features of fuel constituent migration can be summarized as follows: Zirconium migrates to the hotter central region where the bcc γ -phase dominates and to the colder peripheral region that shows a two-phase structure $\alpha + \delta$ or $\delta + \zeta$ from the intermediate region that shows a two-phase structure such as $\gamma + \zeta$. As a result, the hotter central region shows a γ single phase with a Zr content of >40 at.%, and the intermediate region becomes the ζ single phase with a Zr content of 2–5 at.%. Uranium migrates in the opposite directions of the Zr migration. Plutonium does not show significant redistribution. When the central region temperature is relatively low ($<\sim 930$ K) where a γ single phase does not form, Zr in the central region migrates out to the peripheral region. Although the specific migration rate has not been evaluated, marked redistribution has been observed in the U–Pu–Zr fuel slug at about 2 at.% burnup.

In MA-bearing metal fuel, redistribution of Am has been observed.^{58–60} Am-rich precipitates were uniformly distributed in the as-fabricated fuel. However, the Am-rich precipitates disappeared from the intermediate region, as shown in Figure 21.⁶⁰

Fuel constituent migration is considered to be caused by a radial gradient of the chemical potential of the fuel constituent. This phenomenon is known as ‘thermodiffusion.’ Models^{86–88} have been proposed in order to understand fuel constituent migration, as described in Chapter 3.23, Metal Fuel Performance Modeling and Simulation.

Fuel constituent migration affects the local solidus temperature and thermal conductivity of the fuel slug. However, calculation indicates only a minor influence of the thermal conductivity change on the slug temperature radial profile.^{90,91}

3.01.4.3 Fission Gas Release and Gas Swelling

In the early stage of irradiation (<1 at.% burnup), most of the gas atoms generated by fission stay in the fuel slug and form gas bubbles. This leads to a large swelling of the fuel slug at this stage. In the low smear density (<75%) fuel pin, where about 40 vol.% or larger swelling is allowed, further irradiation increases the population and volume of the bubbles, and causes coalescence among them. Progression of the coalescence leads to the formation of open pores that are

Table 6 Representative irradiation test assemblies in the IFR program

<i>Test assembly no.</i>	<i>X419, X420, X421</i>	<i>X423</i>	<i>X425</i>	<i>X430</i>	<i>X441</i>	<i>X447</i>	<i>IFR-1</i>	<i>MFF-2</i>
Remark	Lead tests	Swelling behavior	Lead tests	Large diameter, high Pu	Code benchmark, high smear density	High temp.	Full length	Full length, U-Zr
Reactor for irradiation	EBR-II	EBR-II	EBR-II	EBR-II	EBR-II	EBR-II	FFTF	FFTF
Fuel alloy composition (wt%)	U-10Zr, U-xPu- 10Zr ($x = 8, 19$)	U-10Zr, U-xPu- 10Zr ($x = 3, 8,$ $19, 22, 26$)	U-10Zr, U- xPu-10Zr ($x = 8, 19$)	U-10Zr, U-xPu-10Zr ($x = 19, 22, 26$)	U-19Pu-yZr ($y = 6, 10, 14$)	U-10Zr	U-10Zr, U-xPu- 10Zr ($x = 8, 19$)	U-10Zr
Cladding material	D9	316SS	HT9	HT9	HT9, D9	HT9	D9	HT9
Cladding outer diameter (mm)	5.84	7.37	5.84	7.37	5.84	5.84	6.86	6.86
Cladding thickness (mm)	0.38	0.41	0.38	0.41	0.38	0.46	0.56	0.56
Fuel slug outer diameter (mm)	4.32	5.66	4.32	5.66	5.71		4.98	4.98
Fuel slug length (mm)	343	343	343	343	343	343	914	914
Fuel smear density (%)	72	75	72	75	70,75, 85	75	75	75
Plenum/fuel volume ratio	1	1	1	1.4	1.1,2.1	1.4	1.2	1.3
Peak linear power rate (W cm ⁻¹)	394	427	482	492	459	361	492	541
Peak cladding temp. (°C)	590	522	590	540	600	660	615	618
Peak burnup	18.4 at.%	4.9 at.%	19.3 at.%	11.5 at.%	12.7 at.%	10 at.%	94 GWdt ⁻¹	94 GWdt ⁻¹

Table 7 Irradiation tests of MA-bearing metal fuel

	<i>X501</i>	<i>METAPHIX</i>	<i>AFC-1B</i>	<i>AFC-1F,-1H</i>	<i>AFC-2A,-2B</i>	<i>FUTURIX-FTA(Metal)</i>
Reactor for irradiation	EBR-II	Phenix	ATR	ATR	ATR	Phenix
Fuel alloy composition (wt%)	U-20.2Pu-9.10Zr-1.2Am-1.3Np	U-19Pu-10Zr U-19Pu-10Zr-2MA-2RE U-19Pu-10Zr-5MA-5RE U-19Pu-10Zr-5MA (MA: Np, Am, Cm) (RE: Y, Ce, Nd, Gd)	Pu-12Am-40Zr Pu-10Am-10Np-40Zr Pu-60Zr Pu-40Zr	U-29Pu-4Am-2Np-30Zr U-34Pu-4Am-2Np-20Zr U-25Pu-3Am-2Np-40Zr U-28Pu-7Am-30Zr	U-20Pu-3Am-2Np-1.0RE-15Zr U-20Pu-3Am-2Np-1.5RE-15Zr U-30Pu-5Am-3Np-1.5RE-20Zr U-30Pu-5Am-3Np-1.0RE-20Zr U-30Pu-5Am-3Np-20Zr (RE: La, Pr, Ce, Nd)	U-20Pu-3Am-2Np-15Zr Pu-12Am-40Zr
Fuel slug O.D. (mm)	4.27	4.9	4.01	4.01	4.27	
Fuel slug length (mm)	343	485 (100 of MA section)	38.1(25.4 for Pu-60Zr)	38.1	38.1	
Cladding material	HT9	15-15Ti	HT9	HT9	HT9	
Cladding O.D. (mm)	5.84	6.55	5.84	5.84	5.84	
Peak linear power rate (W/cm^{-1})	450	350	330 (design limit)	330 (design limit)	350	272 (low-fertile) 320 (nonfertile)
Peak cladding temp. (K)	813	845	823 (design limit)	823 (design limit)	823 (design limit)	
Peak burnup (at.%)	7.6	2.5,7,11	4-8	4-8 (1F), 35-40 (1H)	>10(2A), >25(2B)	7.0 (low-fertile) 11.4 (nonfertile)

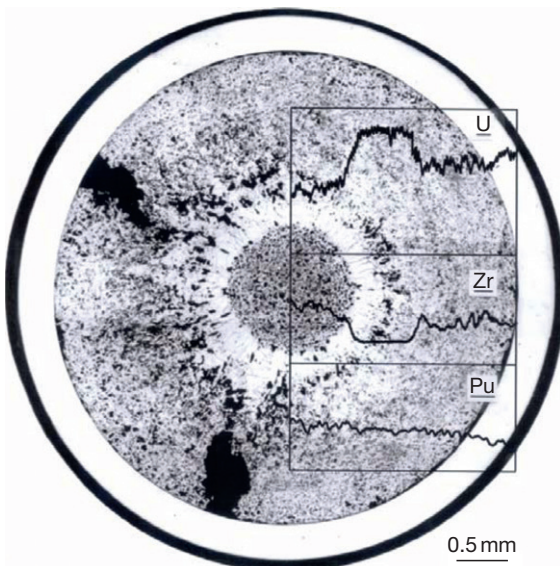


Figure 20 Optical micrography and measured constituent redistributions of U-19 wt% Pu-10 wt% Zr fuel at 1.9 at.% burnup. Reproduced from Kim, Y. S.; Hofman, G. L.; Hayes, S. L.; Sohn, Y. H. *J. Nucl. Mater.* **2004**, 327, 27.

connected to the outside of the fuel slug.^{4,69,70} Interconnection of the bubbles with cracks and cavities may also occur and contribute to open pore formation. The fission gas included in the bubbles is released through the open pores. **Figure 22** presents irradiation test data on fractional fission gas release⁶⁷ (the ratio of cumulative released fission gas atoms to cumulative generated fission gas atoms) versus fuel volume increase for U-Fs, U-Pu-Fs, and U-Pu-Zr fuel, showing that fission gas release starts abruptly when the fuel slug volume increase reaches 20–30%, independently of the fuel alloy composition, burnup, and irradiation temperature. These data are consistent with the prediction model of Barnes⁹²; the interconnection among the bubbles readily occurs at 33.3 vol.% swelling (break-away swelling). The fission gas release versus fuel burnup data^{93–95} for U-Zr and U-Pu-Zr fuel are presented in **Figure 23**. Gas release starts at about 1 at.%, which presumably corresponds to the break-away swelling, increases with burnup, and then asymptotically approaches 70–80%. This behavior is independent of the Pu content and the fuel slug length. (Note that **Figure 23** contains the data for the full-length fuel pin irradiated in FFTF.⁹⁵) Around the time of fission gas release onset, the swollen fuel slug touches the inside of the cladding, but further swelling is suppressed because of gas release.

In the case of the high smear density (>85%) fuel pin, the fuel slug swelling is restrained by the

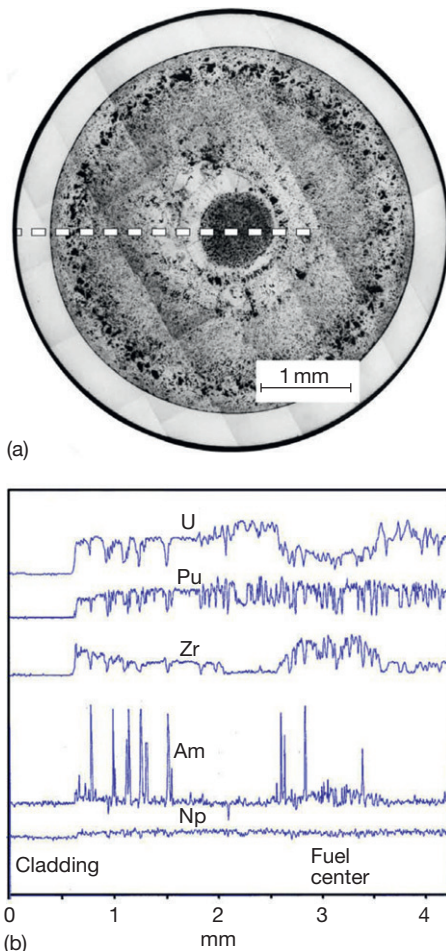


Figure 21 (a) Optical micrography of MA-bearing metal fuel pin from X501 test and (b) measured constituent redistributions along the scan direction indicated by the broken line in (a). Reproduced from Kim, Y. S.; Hofman, G. L.; Yacout, A. M. *J. Nucl. Mater.* **2009**, 392, 164.

cladding before bubble interconnection is fully developed.⁹ Accordingly, fission gas release stays at a lower level. The 85% smear density fuel pin in the X441 test assembly showed a fractional fission gas release of 57% at a peak burnup of 11 at.%,⁹ as shown in **Figure 23**.

Pahl *et al.*⁶⁸ assumed a mild temperature dependence of fission gas release, based on their data of Kr and Xe retained in the slug showing a relatively flat axial profile.

The behavior of the helium that is generated associated with the transformation of MA is the focus of recent irradiation tests of MA-bearing metal fuel. The data for the X501,⁵⁹ METAPHIX,⁷⁶ and AFC-1⁷⁸ tests consistently show that fractional release of He is higher than those of Xe and Kr.

3.01.4.4 Restructuring and Deformation of the Fuel Slug

The swelling mechanisms of metal fuel slugs include fission gas bubble formation, irradiation growth, grain boundary cavitation, and cracking.^{3,4,69} A cross section of an irradiated fuel slug, as can be seen in Figures 20 and 24,⁶⁰ exhibits a two- or three-ring structure, and each ring (or annular region) shows a

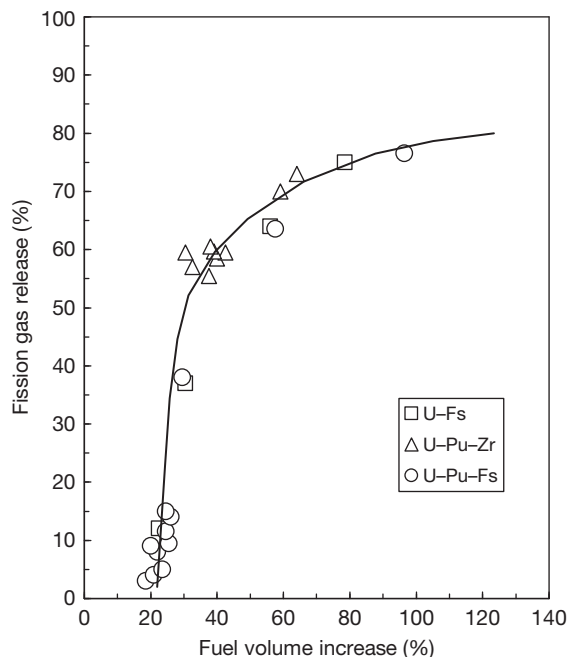


Figure 22 Fractional fission gas release versus fuel volume increase.

characteristic appearance.⁶⁹ In the central γ -phase region, spherical gas bubbles⁶⁹ can be found. The pores in the low-temperature peripheral region are characterized by a highly distorted configuration,^{3,69} which are associated with grain boundary tearing and cavitation void swelling (bias-driven void swelling).⁹⁶ It is well known that orthorhombic α -uranium crystals exhibit anisotropic irradiation growth.³ Therefore, the grain boundaries in the randomly oriented polycrystalline fuel alloy that contains an α -phase are torn after irradiation.³ Hofman and Walters,³ Hofman *et al.*,⁶⁷ and Pahl *et al.*⁶⁸ suggest the influence of a preferred grain orientation or texture induced by stress or temperature gradients during manufacture or in-reactor operation. Large radial cracks occur at the low-temperature peripheral region of the U–Pu–Zr fuel slug, as shown in Figure 20. The intermediate ζ -phase region, where Zr is depleted, appears to be dense in Figure 20, but contains uniformly distributed fine spherical bubbles, as indicated in Figure 24. When the central region temperature is relatively low ($<650\text{--}700^\circ\text{C}$), where the γ single phase does not form, a Zr-depleted region is formed in the central part of the slug, and the cross section shows a two-ring structure. This restructuring (ring structure formation) precedes fuel constituent migration according to Porter *et al.*,⁸⁴ but it may be possible that the constituent migration affects the restructuring.

Figures 25–27 present irradiation test data of fuel slug axial elongation.^{67,93,97} After rapid swelling in the early stage ($\sim 2\text{ at.\%}$), the elongation levels off at an asymptotic value of 4–10%, depending on the

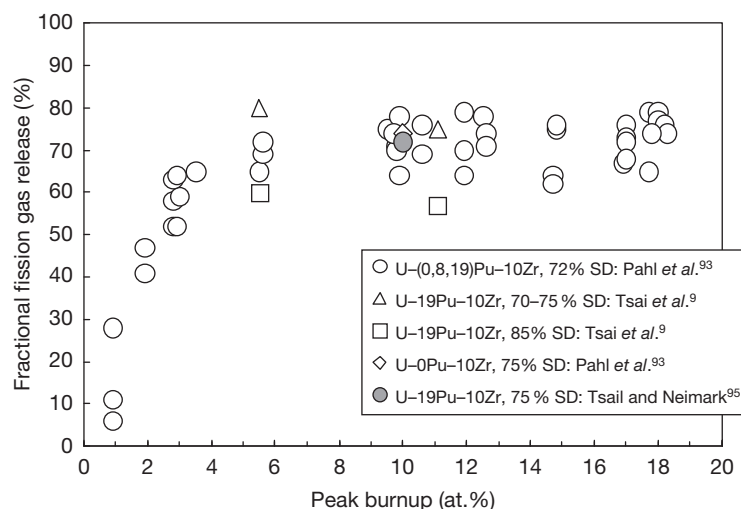


Figure 23 Fractional fission gas release peak burnup.

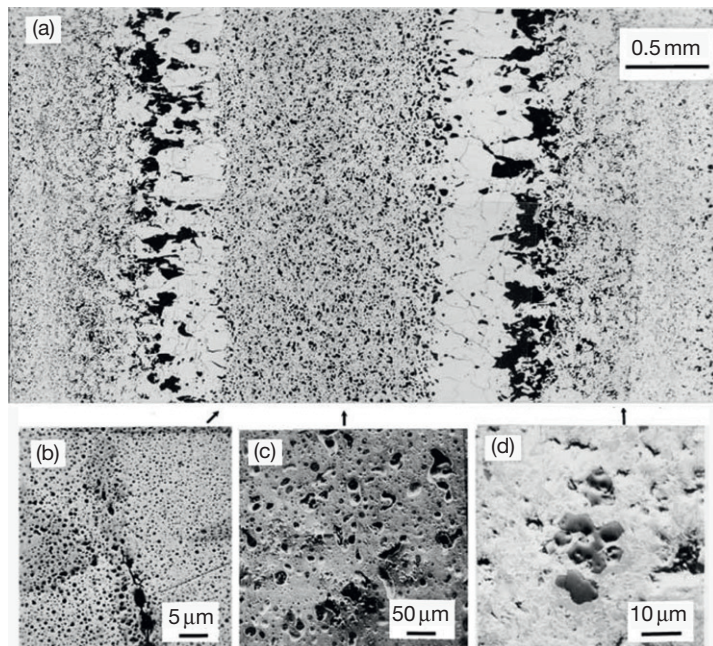


Figure 24 Pore morphology of irradiated U-Pu-Zr fuel shown by optical metallography and SEM images: (a) optical micrograph of axial cross section, SEM images of (b) intermediate zone, (c) central zone, (d) outer zone. Reproduced from Kim, Y. S.; Hofman, G. L.; Yacout, A. M. *J. Nucl. Mater.* **2009**, 392, 164.

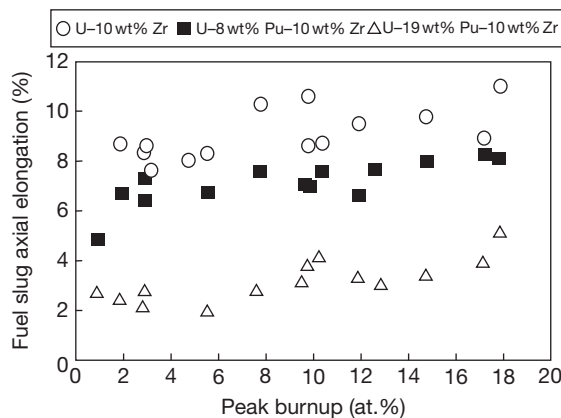


Figure 25 Fuel slug axial elongation versus peak burnup for test assemblies X419-421 (fuel slug diameter: 4.32 mm, see Table 6). Data from Pahl *et al.*⁹³

Pu content and the diameter of the fuel slug. This leveling off is due to the restraint by the cladding after contact of the swollen fuel slug with the inside of the cladding.⁶⁹ In a fuel pin of smear density SD (%), fuel slug radial deformation $[(100/SD)^{1/2} - 1] \times 100$ (%) of the fuel slug causes contact with the cladding; for example, in a fuel pin of 72–75% smear density, slug radial deformation at contact is 15–18%. Therefore, the test data in Figures 25–27 mean that the fuel deforms more in the radial direction than in the axial direction. This anisotropic

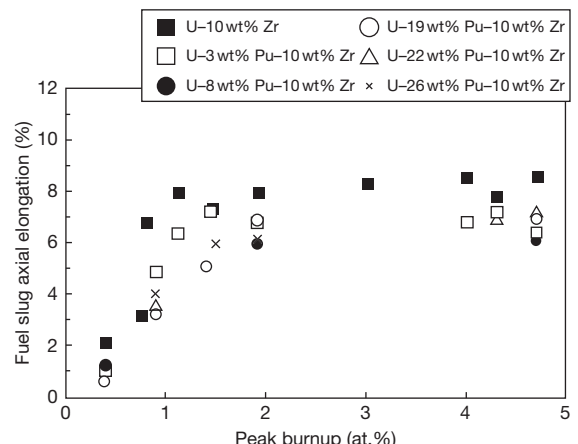


Figure 26 Fuel slug axial elongation versus peak burnup for test assemblies X423 (fuel slug diameter: 5.66 mm, see Table 6). Data from Hofman *et al.*⁶⁷

deformation may be attributed to the stress state of a whole fuel slug, which is similar to that of a thin cylindrical shell subjected to internal pressure⁶⁹; the radial-to-axial stress ratio in the shell is about 2:1. This idea is based on the assumption that the central hotter part of the slug swells at a higher rate than the peripheral colder part, where the creep rate of the slug is small.⁶⁹ In fact, extrusion of the slug's inner part into the radial crack in the peripheral region was observed in an irradiated metal fuel cross section.⁶⁹

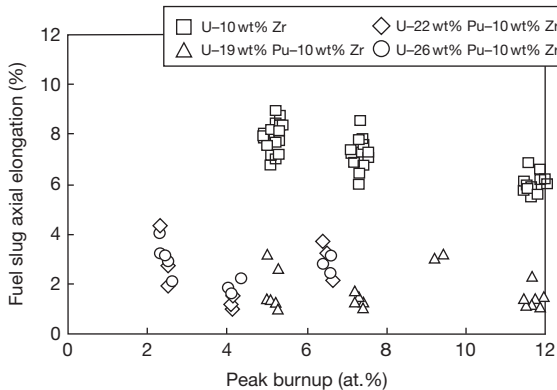


Figure 27 Fuel slug axial elongation versus peak burnup for test assemblies X430 (fuel slug diameter: 5.66 mm, see [Table 6](#)). Data from Crawford *et al.*⁹⁷

This suggests that the inner part of the slug swells at a higher rate than the peripheral part. Other factors that cause anisotropic deformation may be grain boundary tearing, cavitation void swelling, and/or cracking in the peripheral region. The fuel slug axial elongation data shown in [Figures 25–27](#) also indicate the dependency on the Pu content and fuel slug diameter; higher Pu and smaller diameter slugs show more anisotropic deformation (less axial elongation).⁶⁷ This trend can be attributed to cracking and irradiation growth in the peripheral region explained by Hofman *et al.*,⁶⁷ fuel slugs of high Pu content (~ 20 wt%) are brittle so that radial cracking occurs in the early stage of irradiation, as can be seen in [Figure 20](#); radial cracking accelerates the time of slug–cladding contact, thereby suppressing the axial elongation. A proposed model correlates the anisotropic deformation with the Pu content and the radial temperature gradient of the fuel slug.⁹⁸

Incompressible swelling due to the accumulation of solid fission products may not contribute the fuel slug swelling at a low burnup, but causes FCMI at a higher burnup, as discussed later.

3.01.4.5 Fuel–Cladding Mechanical Interaction

Increase in gas bubble swelling is suppressed after the onset of fission gas release. If the fission gas release precedes the fuel slug–cladding contact, mechanical interaction between the fuel slug and cladding (FCMI) will be at a low level. This is true for fuel pins of lower (<75%) smear density. In this case, cracks and open pores, if any, can accommodate the gas swelling increase; the slug's inner part can be extruded into the radial crack in the peripheral

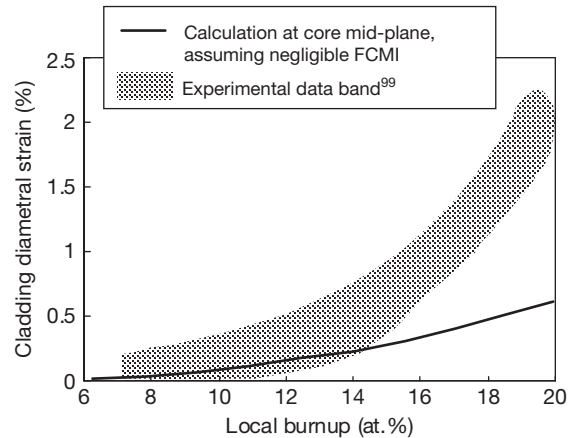


Figure 28 Cladding diametral strain of HT-9-clad U–Pu–Zr fuel pins of smear density 75%.

region, as reported in Hofman *et al.*⁶⁷; the open pores may collapse when compressed, because they do not contain high-pressure gas unlike gas bubbles.⁹⁸ Accordingly, FCMI does not increase as long as there is a sufficient volume of cracks and/or open pores. [Figure 28](#) shows the trend of cladding diametral strain data for the fuel pins of 75% smear density with swelling-resistant, ferritic/martensitic steel HT9 cladding.⁹⁹ The curve in the figure is the cladding diametral strain calculated assuming negligible FCMI. Comparison of the curve with the data trend suggests that FCMI does not occur until about 10 at.% burnup.

However, [Figure 28](#) also suggests a gradual buildup of FCMI at a higher burnup exceeding ~ 10 at.%. This FCMI buildup can be attributed to incompressible volume increase due to solid fission product accumulation (solid fission product swelling). The rate of solid fission product swelling can be estimated from the fission yield. The upper-bound rate of solid fission product swelling, 1.5 vol.%/at.%, can be calculated by assuming that all the fission products except the noble gas contribute to it.⁹⁸ Hofman and Walters³ have estimated the solid fission product swelling rate to be 1.2 vol.%/at.% by considering dissolution of alkali and alkaline-earth elements into bond sodium.

In the case of the fuel pins of 85% smear density, excessive FCMI causes significant cladding strain (as large as $\sim 2\%$ until 10 at.%) as indicated in [Figure 29](#).¹⁰⁰ In 85% smear density fuel pins, the volume of cracks and/or open pores is lower so that it is consumed earlier by solid fission product buildup than in 75% smear density pins.

[Figure 30](#)¹⁰⁰ presents the axial profile of cladding diametral change of HT-9-clad U–Pu–Zr fuel pins at

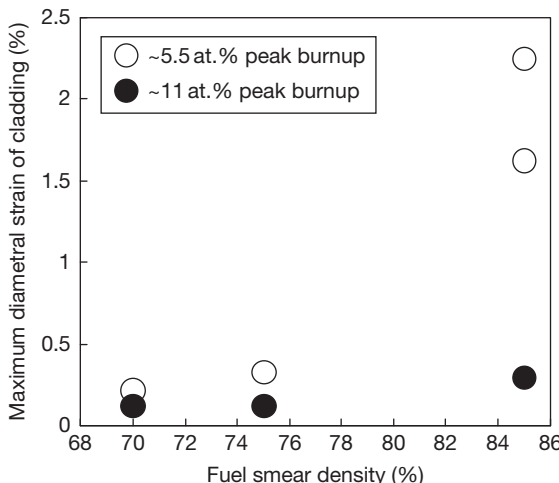


Figure 29 Maximum cladding diametral strain versus fuel smear density for HT-9-clad U-Pu-Zr fuel pins.

a peak burnup of 15–16 at.%. The cladding diameter increase peaks at the middle of the fuel slug and is lower at the both ends, similar to the local burnup profile, that is, solid fission product swelling distribution. FCMI may be at a lower level, particularly in the high-temperature upper part of the slug, because there is less solid fission product swelling and cracks and/or open pores can easily collapse at a lower compression stress due to its higher creep rate. The cladding diametral change profile may reflect this FCMI behavior.

The FCMI behavior described above is for swelling-resistant steel cladding. In the case of austenitic steel cladding, lower FCMI is predicted because irradiation swelling of the cladding increases the cladding diameter.

3.01.4.6 Change in Fuel Slug Temperature

The formation of gas bubbles and cavitation at the beginning of irradiation degrades the effective thermal conductivity of the fuel slug.^{3,4} When open pores are formed as a result of the interconnection among the bubbles, fission gas inside of the bubbles comes out through the open pores and the bond sodium goes into some of the open pores.^{3,4} Partial infiltration of the bond sodium recovers the degraded effective thermal conductivity of the slug.^{3,4} This change in thermal conductivity is supported by the temperature measurements for the slugs in instrumented fuel pins.^{101,102} Bauer and Holland¹⁰³ evaluated the effect of bond sodium infiltration on slug thermal

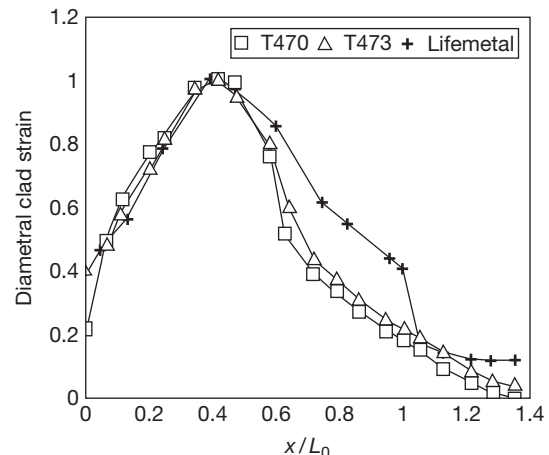


Figure 30 Cladding diametral strain profiles of HT-9-clad U-19 wt% Pu-10 wt% Zr fuel pins at 15.5 at.% (T473) and 15.9 at.% (T470) peak burnups.

conductivity from the radii of the molten region of the irradiated fuel slugs subjected to the transient overpower tests, as follows:

Before sodium infiltration

$$k_{\text{eff}} = k_0 (1 - P_g)^{(3/2)\varepsilon} \quad [7]$$

and after sodium infiltration

$$k_{\text{eff}} = k_0 \left[1 - 3 \frac{1 - k_{\text{Na}}/k_0}{2/\varepsilon + (3 - 2/\varepsilon)(k_{\text{Na}}/k_0)} \cdot \frac{P_{\text{Na}}}{1 - P_g} \right] \cdot (1 - P_g)^{3/2} \quad [8]$$

where k_{eff} is the effective thermal conductivity of the irradiated fuel slug ($\text{W m}^{-1} \text{K}^{-1}$), k_0 is the thermal conductivity of the unirradiated fuel slug ($\text{W m}^{-1} \text{K}^{-1}$), k_{Na} is the thermal conductivity of sodium ($\text{W m}^{-1} \text{K}^{-1}$), P_g is the volume fraction of gas-filled pores, P_{Na} is the volume fraction of sodium-filled pores, and ε is a constant ($\varepsilon = 1.72$). According to eqn [7], for example, the effective conductivity of the fuel slug attaining 40% gas swelling without any sodium infiltration decreases down to 40–50% of the unirradiated slug.

3.01.4.7 Fuel-Cladding Chemical Interaction

Part of lanthanide fission products agglomerate at the peripheral region of the fuel slug and react with the inside of the cladding.^{3,68,71,93} The reaction region of the cladding is so brittle^{3,70} that it should be regarded as wastage. Above a threshold temperature, a liquid phase is formed at the interface between the fuel slug

and the cladding as a result of interdiffusion among the fuel and cladding constituents.^{11,104,105} These reactions between the fuel slug side and the cladding side is called fuel–cladding chemical interaction (FCCI). FCCI is a complicated multisystem reaction involving fuel constituents, cladding constituents, impurity elements in the fuel and cladding, and fission products. FCCI during steady-state irradiation described in this subsection is dominated by the reaction of lanthanide fission products with the cladding. The reaction accompanied by liquid-phase formation is caused under transient conditions; so this is explained in the next section. Detailed description is provided in Chapter 3.15, Metal Fuel–Cladding Interaction.

The lanthanide-rich wastage layer inside the cladding consists of intermetallic compounds between lanthanides and cladding constituents, such as $\text{Fe}_{17}\text{Nd}_2$ and Fe_2Ce , considering relevant elemental binary alloy phase diagrams.³⁷ Recent out-of-pile isothermal diffusion tests by using lanthanide alloy/Fe–Cr alloy diffusion couples revealed that the reaction zones consisted of some of these intermetallic compounds.¹⁰⁶ It has been reported that Pd is contained in the lanthanide-rich wastage layer in irradiated fuel pins.⁹³ The features of the wastage layer vary with the type of cladding steel used. The wastage layer in austenitic steel cladding is characterized by Ni depletion.^{3,68,71,93,95} In the ferritic steel cladding, a decarburized zone is formed at the wastage front.^{3,9,94} A certain amount of U and Pu is contained in the wastage layer for both types of cladding.^{9,71,95} The thickness of the wastage layer is not circumferentially uniform.⁹⁴ This nonuniformity may be associated with localized agglomeration of lanthanide fission products at the pores and cracks in the fuel slug.

The maximum wastage layer thickness tends to increase with increasing local burnup and local temperature,¹¹ as shown in Figure 31. The figure presents the data for the wastage in the U–Pu–Zr fuel pins clad with HT-9 steel. When the U–Zr fuel pins clad with HT-9 were irradiated at a peak cladding temperature of 660 °C, cladding failure occurred at 9.5 at.% burnup and a 170-μm thick wastage zone was found at the failure site.⁹⁴ This extensive wastage was considered to have been caused during operation beyond the cladding breach; the loss of bond sodium from the breach site raised the fuel slug temperature, promoted the supply of lanthanides, and accentuated the wastage.⁹⁴ The maximum wastage for unbreached fuel pins was less than 100 μm.⁹⁴

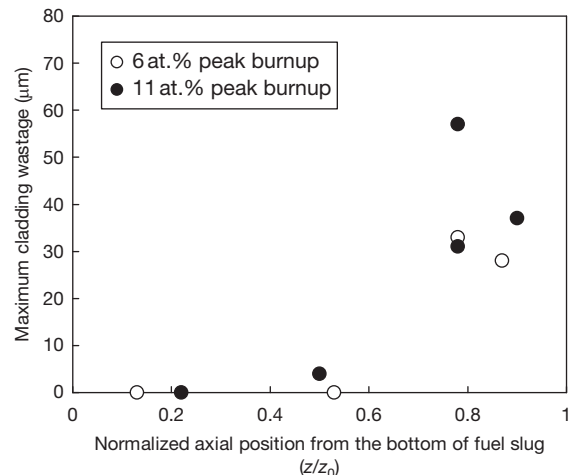


Figure 31 Maximum cladding wastage thickness at various axial positions for HT-9-clad U–Pu–Zr fuel pins. Data are from Cohen et al.¹¹ The axial position is normalized by fuel slug length.

Evolution of the wastage may be controlled by migration of lanthanide fission products to the peripheral region of the fuel slug. The mechanism of migration may be vapor transport through the open pores⁹⁵ and/or thermodiffusion, but this has not yet been determined.

There has been the idea of ‘lined cladding’ for protection against FCCI. This is to place a relatively inert material such as a refractory metal inside the cladding. In-pile⁶⁸ and out-of-pile^{107–110} tests have been conducted to check the feasibility of lined cladding.

3.01.4.8 Behavior of Fission Products

Elements of high fission yield in a fast reactor neutron spectrum are noble gas (25%), lanthanides (45%), alkali and alkaline-earth elements (Ba, Cs, and Sr: 30%), noble metals (Tc, Ru, Rh, and Pd: 50%), and others (Zr and Mo: 40%).⁹⁸ Noble gas forms gas bubbles and causes gas swelling. A major part (~80%) of the noble gas is finally released from the fuel slug and accumulates in the gas plenum, as described in Section 3.01.4.3. Lanthanide elements do not dissolve in the fuel alloy, as suggested from the binary alloy phase diagrams³⁷ (also see Chapter 2.05, Phase Diagrams of Actinide Alloys). Part of the lanthanide elements precipitate in the pores and cracks in the peripheral region of the slug, and react with the inside of the cladding.^{3,69,70} Significant amounts of alkali and alkaline-earth elements are considered to dissolve in the bond sodium,³ and the

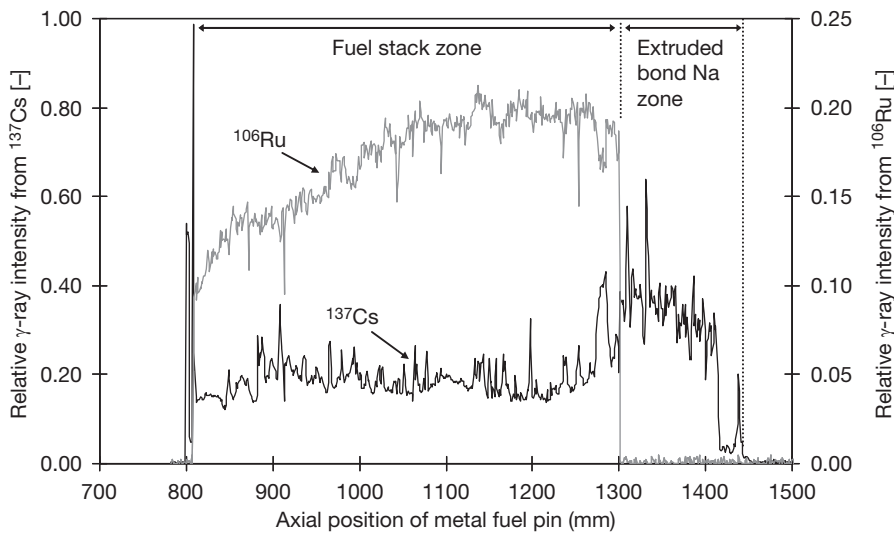


Figure 32 ^{137}Cs and ^{106}Ru γ autoradiography of 2.5 at.% peak burnup U–Pu–Zr fuel pin from the METAPHIX test.

remaining part may precipitate in the fuel slug as a result of the very low solubility of these elements in U and Pu. In fact, the γ (from ^{137}Cs and ^{106}Ru) autoradiography of an irradiated metal fuel pin⁷⁵ presented in **Figure 32** indicates the transfer of Cs to the bond sodium in the plenum region. According to the binary alloy phase diagrams³⁷ (also see **Chapter 2.05, Phase Diagrams of Actinide Alloys**), noble metals form intermetallic compounds with U and Pu, and Zr and Mo dissolve in U and Pu. **Figure 32** also shows that the Ru distribution is similar to the burnup profile, which means that Ru is immobile.

Based on the above consideration, Zr, Mo, Tc, Ru, Rh, and Pd of fission products will affect the solidus temperature of U–Zr and U–Pu–Zr fuel alloys. The effect of the fission products on the solidus temperature can be estimated as follows⁹⁰: When 1 wt% of heavy metals (U and Pu) fission, the total production of Zr, Mo, Tc, Ru, Rh, and Pd is 0.36 wt% of the initial heavy metal. A breakdown of the production is shown in **Table 8**. Studies on U–Pu–Fz alloys were performed in the United States,^{22,26} where Fz stands for fizzium, the alloy of Zr, Mo, Ru, Rh, and Pd having the composition²² shown in **Table 8**. The Fz composition is similar to the fission yield shown in **Table 8**. Therefore, the effect of fission product accumulation on the solidus temperature of U–Pu alloys can be assumed to be the same as that of Fz addition. The solidus temperatures of U–Pu and U–Pu–10 wt% Fz alloys have been reported, and are shown in **Table 9**.²² The solidus temperatures of the U–Pu alloys, the compositions of which are calculated by subtracting

Table 8 Fission yield of Zr, Mo, Tc, Ru, Rh, and Pd, compared with composition of Fizzium (Fz)

Element	Fission yield (wt%) ^{90,98}	Composition of Fz (wt%) ²²
Zr	19.7	28
Mo	23.9	27.5
Tc	6.3	0
Ru	23.1	29.5
Rh	7	5
Pd	20	10

Fz from the U–Pu–10 wt% Fz alloys, are calculated by using eqn [1], as shown in **Table 9**. The table indicates that 10 wt% Fz addition decreases the solidus temperature of U–Pu alloys by \sim 100 K. Assuming that the decrease in the solidus is proportional to the amount of Fz addition, 0.36 wt% Fz addition leads to a decrease of 3.6 K in the solidus temperature of U–Pu alloys. Therefore, it can be estimated that the effect of burnup on the solidus temperature of the fuel slug is 3.6 K/at.%.

3.01.4.9 Behavior of Breached Fuel Pins

As can be understood from the use of bond sodium, fuel alloys show good compatibility with sodium. Even when a metal fuel pin is breached, the fuel slug does not react with the sodium reactor coolant and the breach site is not enlarged. On the other hand, oxide fuel pellets react with the sodium reactor coolant and form low-density reaction products,

Table 9 Solidus temperatures of U–Pu–Fz and U–Pu alloys

Composition (wt%)	<i>U</i> -10 <i>Pu</i>	<i>U</i> -10 <i>Pu</i> -10 <i>Fz</i>	<i>U</i> -15 <i>Pu</i> -10 <i>Fz</i>	<i>U</i> -20 <i>Pu</i> -10 <i>Fz</i>
Solidus temperature of U–Pu–Fz alloys (°C) ²²	1025	910	865	820
Composition, Fz-subtracted (wt%)	U-10Pu	U-11.1Pu	U-16.7Pu	U-22.2Pu
Solidus temperature of U–Pu alloys by eqn [1] (°C)	1026	1015	964	919

which enlarge the breach site. In order to confirm the benign behavior of breached metal fuel pins, a number of run-beyond-cladding-breach (RBCB) tests^{3,4,111} were conducted in EBR-II. In the tests, the claddings of irradiated fuel pins were thinned mechanically to promote cladding breach, and were then reinserted into the reactor. The results of these tests confirmed the following benign behavior of breached metal fuel pins.^{3,4,111}

At the time of cladding breach, bond sodium and fission gas were expelled through the breach site. Delayed neutron (DN) precursors came out along with the bond sodium, and a short DN signal was detected by a monitoring system. The cesium dissolved in the bond sodium was also expelled. The fission gas released into the reactor coolant was monitored. After the expulsion of bond sodium and fission gas, fission gas expulsion was detected intermittently. The crack at the breach site remained small even over 54–233 days of RBCB operation, because the fuel pin was depressurized and FCMI was kept at a low level. The weight loss of the breached fuel pin was accounted for by the expulsion of the bond sodium, cesium, and fission gas; fuel loss was negligible. The HT-9 cladding fuel pin (13.5 at.% burnup) exhibited crack extension and widening to some extent, but no fuel alloy was extruded over 150 days of RBCB operation.

As described in **Section 3.01.4.7**, the expulsion of bond sodium from the breach site would deteriorate the thermal conductivity of the fuel slug and raise the fuel slug temperature. This may promote the supply of lanthanides and intensify the wastage.⁹⁴ In fact, cladding wastage by lanthanide fission products after 150–200 days of RBCB operation was approximately twice that in unbreached fuel pins at comparable burnup and cladding temperature.⁴

3.01.4.10 Behavior of MA-Bearing Metal Fuel

U–Pu–10 wt% Zr fuel pins containing less than 5 wt% MA irradiated in the X501⁵⁹ and METAPHIX^{75,76} tests consistently showed microstructure, constituent migration, fission gas release, and fission

product (Cs) behavior similar to those of MA-free U–Pu–Zr fuel pins. This means that the addition of a small amount of MA to the U–Pu–Zr matrix does not affect the irradiation behavior of the fuel. The MA-specific irradiation phenomena observed so far have been Am migration along with uranium and zirconium migration and helium gas release. Am-rich phases were present only in the uranium-depleted central and outer zones after irradiation, as shown in **Figure 21**.⁵⁹ Release of the helium gas produced in MA transmutation was higher than the fission gas release in both the X501⁵⁹ and METAPHIX⁷⁶ tests.

The AFC-1 test result showed that the fission gas release behavior of the nonfertile or low-fertile fuel alloys (see **Table 7**) followed the same trend as that of the U–Pu–Zr-based fuel alloys when correlated with fission density.⁷⁸

One of the issues in MA-bearing fuel performance is FCCI because MA, particularly Am, is expected to behave like lanthanide elements, which react with Fe-based cladding materials. However, no FCCI data are available at this point because the inner cladding temperature in the X501 test was too low (<540 °C) to observe a sufficient level of FCCI. From METAPHIX-2 or METAPHIX-3, FCCI data will be obtained in the future.

3.01.4.11 Factors Controlling Fuel Lifetime

Important factors controlling the lifetime of metal fuel pins of low smear density (<75%) during steady-state irradiation are plenum pressure rise due to fission gas accumulation and cladding wastage by lanthanide fission products. The plenum gas pressure produces circumferential tensile stress in the cladding. The decrease in the effective cladding thickness due to the wastage raises the cladding stress. The cladding at the higher temperature upper part of the fuel slug has lower strength and more wastage than any other part. Accordingly, the margin to cladding failure is minimized at the upper part of the slug. In the irradiation test of U–10 wt% Zr fuel pins clad with HT-9, two fuel pins were breached at

9.5 at.% burnup; both breach sites were at the upper part of the slug.⁹⁴ A maximum wastage of nearly 100 μm in depth was found at the upper part of the slug in the sibling pins.⁹⁴

FCMI may increase at a higher (>10 at.%) burnup, particularly in the case of swelling-resistant ferritic steel cladding. However, no FCMI-induced cladding failure has been found, even in the highest peak burnup of 19.4 at.% attained to date. This is because, as discussed in [Section 3.01.4.5](#), FCMI may be at a lower level at the upper part of the slug, where the margin to cladding failure is minimized. Therefore, FCMI may not be an important factor controlling the fuel lifetime.

3.01.5 Transient Behavior

Metal fuel also shows characteristic behavior in transient conditions. For example, when the cladding temperature exceeds a certain threshold value, the interdiffusion between the fuel slug and cladding causes liquefaction of the diffusion zone and extensive wastage of the cladding inside. The molten fuel slug expands axially because of rapid expansion of the fission gas bubbles without producing excessive cladding stress. These phenomena during transient events are important in evaluating the margin to fuel pin failure and failed fuel pin behavior.

In this section, transient tests for metal fuel are reviewed briefly, the linear-power-to-melting is discussed, and then the transient behavior of metal fuel is described.

3.01.5.1 Transient Tests

A series of tests, called the M-series, was performed at the Transient Reactor Test Facility (TREAT) in ANL-Idaho (currently INL) to study the cladding failure threshold and other safety-related behavior of metal fuel during transient overpower (TOP) events.¹⁰ In the six M-series tests, a total of 15 pre-irradiated fuel pins of U-5 wt% Fs clad with 316SS, U-19 wt% Pu-10 wt% Zr clad with D9, and U-10 wt% Zr clad with HT-9 were subjected to overpower conditions simulating TOP events.¹⁰ The sodium loop that carries two or three fuel pins for each test was installed in TREAT.¹⁰ During an exponential power rise in an 8 s period of the TREAT reactor, the fuel pin power increased up to four times the nominal power, and the peak coolant temperature was about 1200 K.¹⁰ Cladding failure occurred for five fuel pins at nearly four times the nominal

power.¹⁰ Every cladding breach site was located near the top of the fuel slug.¹⁰ Examination of intact fuel pins after the test confirmed that the melting region extended over the upper half of the slug and >90% of the cross section near the top of the fuel slug.^{4,10} The test conditions and the results are summarized in [Table 10](#).^{4,5}

Out-of-pile transient tests were conducted in the whole-pin furnace (WPF) system^{12,104} in the Alpha-Gamma Hot Cell Facility (AGHCF) at ANL-Illinois to evaluate fuel behavior in loss-of-flow (LOF) events, where fuel pin power decreases to a decay heat level and the radial temperature profile in the fuel slug is flattened. In the test, an irradiated fuel pin was put into a 316SS capsule and externally heated in the furnace.¹² The cladding and plenum temperatures were maintained at a constant value in the range of 650–820 °C in the six FM series test.¹¹² In the other test, these temperatures were varied to simulate an LOF event.^{12,112}

Out-of-pile tests in the fuel behavior test apparatus (FBTA)^{12,104,105} in AGHCF were conducted to examine compatibility between the fuel slug and cladding at elevated temperatures by externally heating irradiated fuel pin segments. The test data were helpful in understanding FCCI behavior in metal fuel, particularly liquid-phase formation. Compatibility between the fuel slug and cladding has also been studied by conducting out-of-pile isothermal annealing tests for diffusion couples consisting of unirradiated fuel alloys and Fe-based alloys.^{112–120}

3.01.5.2 Linear-Power-to-Melting

When metal fuel transient behavior is discussed, it may be important to know the linear power required to cause fuel centerline melting, which is called ‘linear-power-to-melting’¹²² for the metal fuel. This subsection describes the method for a conservative evaluation of the linear-power-to-melting.^{90,91}

The linear-power-to-melting for metal fuel is evaluated on the basis of calculations of the temperature distribution and solidus temperature of a fuel slug, which are influenced by fuel specifications, irradiation conditions, and irradiation behavior, such as the fuel alloy composition, smear density, axial linear power profile, inlet coolant temperature, gas swelling, fuel constituent migration, bond sodium infiltration into the swollen fuel slug, and solid fission product accumulation.

The radial temperature distribution at a certain axial position of a fuel slug is calculated by using a

Table 10 Conditions and results of TREAT M-series tests

Test	Fuel composition (wt%)	Cladding	Peak burnup(at.%)	Peak overpower (normalized ^a)	Cladding failure	Maximum axial expansion (%)
M2	U-5Fs	316SS	0.3	4.1	No	16
	U-5Fs	316SS	4.4	4.2	No	Ambiguous
	U-5Fs	316SS	7.9	4.1	Yes	3
M3	U-5Fs	316SS	0.3	4.1	No	18
	U-5Fs	316SS	4.4	4.0	Yes	4
	U-5Fs	316SS	7.9	3.4	No	4
M4	U-5Fs	316SS	Fresh	3.8	No	4 ^c
	U-5Fs	316SS	2.4	4.1	Yes	7
	U-5Fs	316SS	4.4	3.8	No	4
M5 ^b	U-19Pu-10Zr	D9	0.8	4.3	No	1
	U-19Pu-10Zr	D9	1.9	4.3	No	2
M6	U-19Pu-10Zr	D9	1.9	4.4	No	2-3
	U-19Pu-10Zr	D9	5.3	4.4	Yes	3
M7	U-19Pu-10Zr	D9	9.8	4.0	Yes	3
	U-10Zr	HT9	2.9	4.8	No	2-4

Source: Hofman, G. L.; Walters, L. C.; Bauer, T. H. *Prog. Nucl. Energy* **1997**, *31*, 83; Crawford, D. C.; Porter, D. L.; Hayes, S. L. *J. Nucl. Mater.* **2007**, *371*, 202.

^aNormalized by nominal conditions: peak linear power of 40 kW/m, 630 K inlet, and 150 K coolant temperature rise.

^bTest fuel pins were subjected to twice over power transients.

^cExpansion may have been caused by localized sodium bond boiling.

one-dimensional steady-state heat conduction model. The thermal diffusivity of metal fuel is small enough to use the steady-state model even for analysis of overpower reactor events such as the TREAT test. For obtaining a conservative estimate of the fuel slug temperature, the influence of irradiation behavior is treated as follows: The effective thermal conductivity of the fuel slug is calculated from eqn [7], which does not incorporate thermal conductivity recovery due to bond sodium infiltration. Porosity P_g in eqn [7] is conservatively estimated from the smear density and the irradiation data of fuel slug axial elongation. The porosity is assumed to be uniform and constant from the beginning of irradiation. As-fabricated uniform fuel composition is assumed without considering fuel constituent migration, because it has only a minor influence on fuel slug temperature, as stated in Section 3.01.4.2.

A conservative estimate of the solidus temperature is obtained as follows: As a result of fuel constituent migration, Zr is enriched in the high-temperature ($>\sim 970$ K) central region where the bcc γ single phase is formed. The solidus temperature in this region may be higher than that of the as-fabricated fuel slug, but is evaluated on the basis of the as-fabricated fuel composition for conservativeness. On the other hand, a Zr-depleted zone is formed at a temperature range of approximately 860–940 K (in the case of U-20 wt% Pu-10 wt% Zr). The Zr

content of the Zr-depleted zone is assumed to be 2.5 at.% based on the irradiation data,^{84,85,86} and then the solidus temperature of this zone is calculated by using eqn [1]. During irradiation, the solidus temperature may be decreased because of the accumulation of fission products. A solidus temperature decrease rate of 3.6 K/at.% burnup is assumed, as discussed in Section 3.01.4.8.

Figure 33 shows the linear-power-to-melting evaluated in the case of a nominal peak linear power of 380 W cm^{-1} , a peak cladding inner temperature of 923 K, an inlet coolant temperature of 668 K, and a fuel smear density of 75%. For a Pu content of <20 wt%, the linear-power-to-melting of U-Pu-10 wt% Zr fuel is higher than 600 W cm^{-1} . This means that the U-Pu-10 wt% Zr fuel has a sufficient margin to fuel slug melting. As also shown in Figure 33, the U-Pu-3 wt% Zr fuel has a linear-power-to-melting of $>550 \text{ W cm}^{-1}$ for a Pu content of <15 wt%. This indicates that the U-Pu-3 wt% Zr fuel will be feasible for a large-size reactor core from the standpoint of the margin to fuel slug melting.

3.01.5.3 Liquefaction at the Fuel-Cladding Interface

FCCI during steady-state irradiation is dominated by the reaction of lanthanide fission products with the

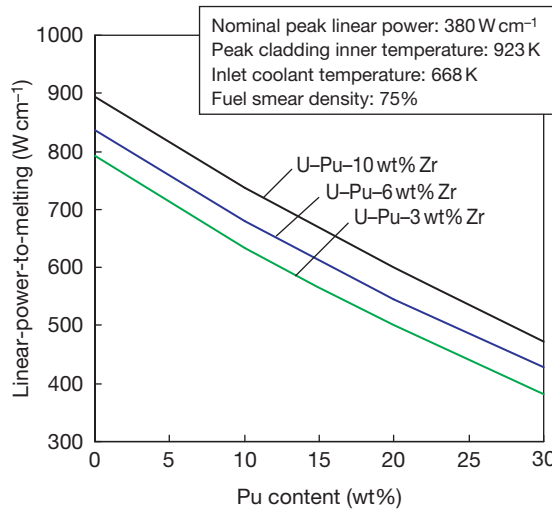


Figure 33 Evaluated linear power to melting.

cladding, as described in [Section 3.01.4.7](#). When the cladding inner temperature exceeds a certain threshold value in transient events, another FCCI mode is initiated; a liquid phase is formed in the reaction zone between the fuel slug and the cladding.^{11,104,105} This liquefaction reaction greatly promotes cladding wastage (liquid-phase cladding penetration).^{11,104} On the other hand, Fe diffusion from the cladding into the fuel slug side causes liquefaction of the peripheral region of the fuel slug.^{11,104} [Figure 34](#)¹¹ shows fission gas bubble coarsening due to the partial liquefaction in the slug peripheral region.

[Figure 35](#)¹¹ presents the data of liquid-phase cladding penetration versus time at 800 °C in the FBTA tests, indicating that the penetration rate decreases with time.¹¹ The cladding penetration rates obtained from 1-h heating data in the FBTA tests were plotted against the inverse temperature, as shown in [Figure 36](#).¹¹ Cladding wastage by lanthanide fission products occurring in high-burnup fuel pins may influence the liquid-phase attack.^{11,104} However, the dependence of liquid-phase cladding penetration on temperature, heating time, and burnup has not yet been quantitatively assessed.

While the maximum heating temperature in the FBTA tests was 800 °C, Bauer *et al.*¹²³ proposed the following relation for the liquid-phase cladding penetration rate, which includes the higher-temperature range.

For $T > 715$ °C,

$$\dot{r} = \exp(22.847 - 27624/T) \quad [9]$$

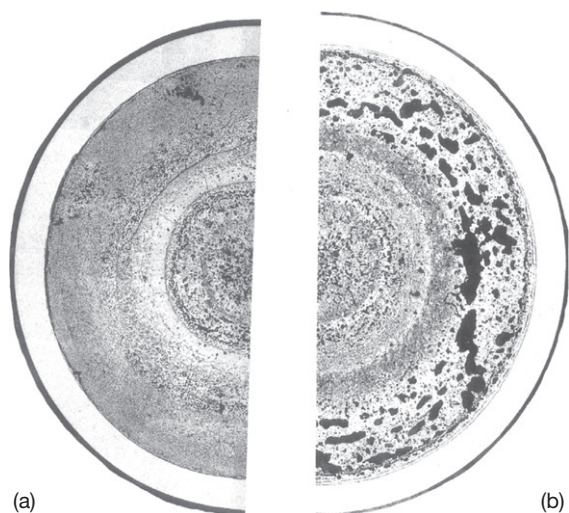


Figure 34 Microstructures of cross-sections of (a) an as-irradiated fuel pin, and (b) a fuel pin after FBTA test, showing partial liquefaction in the fuel slug peripheral region. Reproduced from Cohen, A. B.; Tsai, H.; Neimark, L. A. *J. Nucl. Mater.* **1993**, 204, 244.

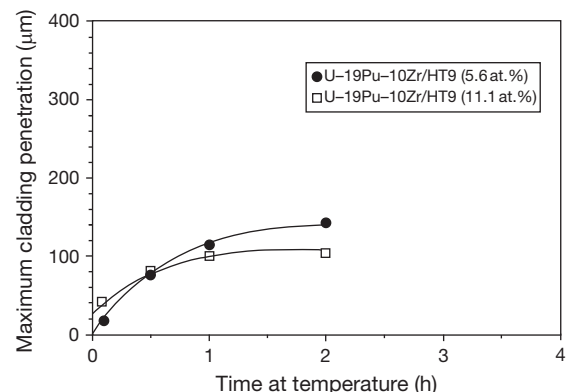


Figure 35 Liquid-phase cladding penetration versus time at 800 °C in the FBTA tests. Reproduced from Cohen, A. B.; Tsai, H.; Neimark, L. A. *J. Nucl. Mater.* **1993**, 204, 244.

except in the range of 1080–1233 °C where

$$\begin{aligned} \dot{r} = & 922 + 2.9265(T - 1388) \\ & - 0.21522(T - 1388)^2 \\ & + 0.0011338(T - 1388)^3 \end{aligned} \quad [10]$$

Here, \dot{r} is the penetration rate ($\mu\text{m s}^{-1}$) and T is the temperature (K). These correlations are based on the results of tests such as dipping tests of Armco iron into molten U-Fe eutectic alloys,¹²⁴ heating tests for irradiated U-5 wt% Fs fuel pins,¹²⁵ and

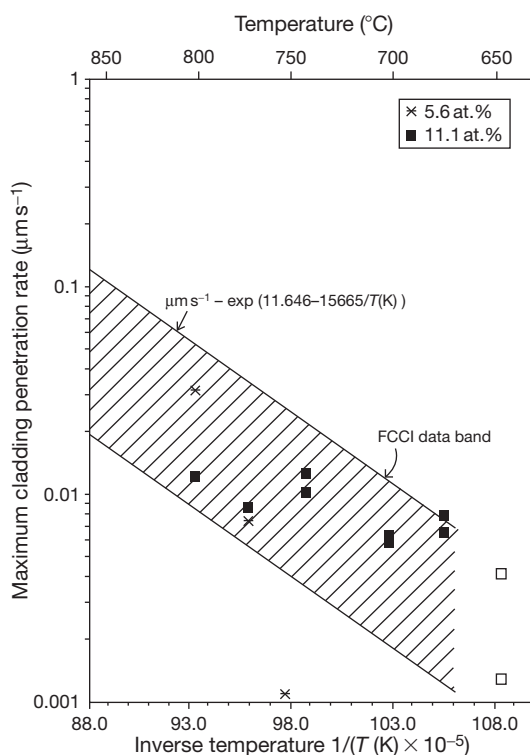


Figure 36 Cladding penetration rates versus inverse temperature, obtained from 1-h heating data in the FBTA tests. Reproduced from Cohen, A. B.; Tsai, H.; Neimark, L. A. *J. Nucl. Mater.* **1993**, 204, 244.

heating tests for D9-clad U–19 wt% Pu–10 wt% Zr fuel pins.¹²³ The accelerated penetration in the intermediate-temperature regime has been attributed to the breakdown of a protective UFe₂ layer between the liquid and the cladding.^{123,124}

According to the FBTA test result, the lowest or threshold temperature for liquid-phase formation in the HT-9-clad U–19 wt% Pu–10 wt% Zr fuel pins was 740–770 °C for 5.6 at.% burnup pins, and 650–675 °C for 11 at.% burnup pins.¹¹ Nakamura *et al.*¹²⁰ summarized the out-of-pile diffusion couple test data^{116–121} including the FBTA test data,¹¹ as shown in **Figure 37**, where the heating temperature is plotted against the Pu/(U + Pu) ratio. The figure suggests that Zr in fuel alloys does not significantly affect the threshold liquefaction temperature, and that liquefaction does not occur at temperatures below 650 °C when Pu/(U + Pu) < 0.25.

The minor influence of Zr in fuel alloys on liquefaction may appear to be inconsistent with the better compatibility of U–Pu–Zr alloys with stainless steels compared to other U–Pu-based alloys, as explained in **Section 3.01.1**. It should be noted,

however, that **Figure 36** indicates the potential of liquid-phase formation but does not provide any information about the penetration rate. The addition of Zr to a fuel alloy will bring about stable intermetallic compounds such as ZrFe₂, which will retard the development of liquid-phase penetration. An important factor that controls the penetration rate is impurities in the fuel alloy and cladding. Hofman *et al.*¹¹³ have pointed out that the formation of a Zr-rich band at the interface between the fuel alloy and steel is induced by the nitrogen in the cladding, hampering the reaction of fuel constituents with steel.

3.01.5.4 Molten Fuel Motion

In a molten part of a fuel slug, fission gas bubbles are coarsened and enlarged as a result of decreased confinement by the fuel alloy matrix and coalescence among the bubbles. This leads to the axial upward extrusion of the molten fuel.¹⁰ Molten fuel extrusion was monitored by the neutron hodoscope during the TREAT M-series tests and observed after the tests.¹⁰ Axial extrusion is important in both reactor core safety and fuel pin integrity in accidental reactor events such as unprotected transient overpower (UTOP). As for the safety, axial fuel expansion provides the reactor core with a large negative reactivity. Regarding fuel pin integrity, fuel melting does not induce significant FCMI. This is because fuel melting starts near the top of the fuel slug due to the high thermal conductivity of metal fuel, so that upward fuel expansion occurs instantaneously upon melting. One might be concerned that shrinkage of the extruded fuel part occurs when the fuel pin power is decreased, resulting in a positive reactivity insertion. However, shrinkage did not occur in the TREAT tests; the posttest radiographs of intact fuel pins were consistent with the result of *in situ* monitoring by the hodoscope.¹⁰ A plausible explanation of the undetectable shrinkage is the irreversibility of coalescence among fission gas bubbles.¹⁰

The amount (length) of extrusion can be estimated by a model balancing the internal pressure of coarsened gas bubbles with plenum gas pressure.¹⁰ A low-burnup fuel pin, in which more fission gas is retained in the fuel slug compared to plenum gas, exhibits large extrusion, as can be seen in the U–Fs fuel data in **Table 10**.

Axial fuel extrusion occurs in the case of not only the fuel slug melting by overheating in a TOP event, but also fuel slug liquefaction by Fe diffusion resulting from FCCI in an LOF event. In the FM-2

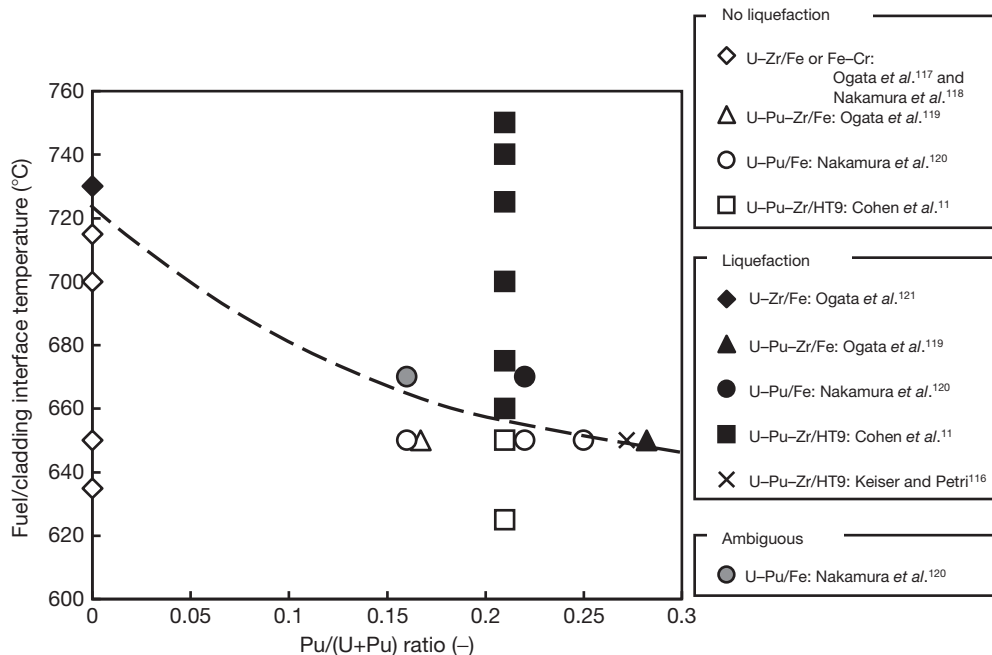


Figure 37 Liquefaction map with respect to temperature and Pu/(U+Pu) ratio.

test with the WPF system, the HT-9-clad U-19 wt% Pu-10 wt% Zr fuel pin of 3.0 at.% peak burnup was heated to 820 °C and was breached 112 min later near the top of the fuel slug.¹² The cross section of this fuel pin at the breach site is shown in Figure 38,¹² indicating that liquefaction covers the whole cross section. In this test, an axial extrusion of 14 mm (4% of the fuel slug length) was measured.¹² This type of liquefaction is not an instantaneous phenomenon because times on the order of minutes are required for a sufficient amount of Fe to diffuse into the fuel slug,¹² whereas the extrusion by fuel slug centerline melting in a TOP event is instantaneous.

3.01.5.5 Fuel Pin Failure Mechanism

Fuel pin failure in transient events is caused by a combination of the plenum gas pressure rise due to coolant temperature increase and FCCI (reaction with lanthanide fission products during steady-state irradiation plus liquid-phase penetration).^{10,12} FCMI is less important even when the fuel slug melts, as stated in the previous section. This mechanism leads to cladding breach near the top of fuel slug, where the cladding strength is lower and FCCI is more significant than in the other cladding part. In fact, every cladding breach in the TREAT M-series tests occurred near the top of the fuel slug.¹⁰ In the FM-series tests in the WPF

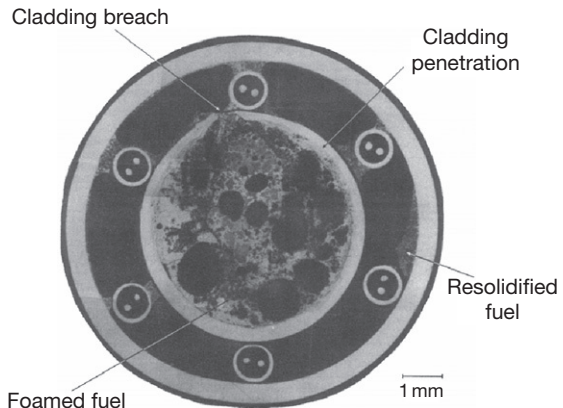


Figure 38 Cross section near the cladding breach site of U-19 wt% Pu-10 wt% Zr fuel pin of 3.0 at.% peak burnup after being held at 820 °C for 112 min (FM-2 test). Reproduced from Liu, Y. Y.; Tsai, H.; Billone, M. C.; Holland, J. W.; Kramer, J. M. *J. Nucl. Mater.* **1993**, 204, 194.

system, three of four failed fuel pins showed cladding breach near the top of the slug¹²; the other failed pin had a breach site at the gas plenum region, the cladding temperature of which was exceptionally higher than that of the fuel slug section.¹²

The dominating factor in the fuel pin failure mechanism will depend on the fuel burnup and the event type. A high-burnup fuel pin will burst as a result of higher plenum gas pressure before liquid-phase

penetration develops. A low-burnup fuel pin will take more time before the cladding bursts, and liquid-phase penetration will develop during that time. In the case of a transient event where the cladding temperature exceeds 1350 K, the accelerated penetration rate as expressed by eqn [10] will cause cladding failure in a very short time.

The HT-9-clad U–10 wt% Zr fuel pin of 2.9 at.% peak burnup exceptionally survived 4.8 times the nominal power transient in the TREAT M-7 test.¹⁰ A cross section of the fuel pin after the test showed less cladding penetration than expected from eqn [10]. One of the reasons for this lower level of penetration could be low interdiffusivity of the elements in the U–10 wt% Zr slugs,¹⁰ as suggested by its high solidus temperature (>1500 K).

3.01.5.6 Failed Fuel Behavior

In the failed fuel pins in the TREAT M-series tests, the molten fuel alloy was ejected rapidly through the breach site and dispersed upward with the coolant.¹⁰ The driving forces of fuel ejection could be expansion of trapped fission gas,¹⁰ bond sodium vapor pressure,¹⁰ and plenum gas flow toward the breach site. The post-failure coolant flow rate was about two-thirds of the prefailure value, indicating only partial flow blockage.¹⁰ Ejection and dispersion of molten fuel alloy were also observed in the FM-series test in the WPF system.¹²

3.01.6 Summary and Future Development

Physical and mechanical property data on U–Zr and U–Pu–Zr alloys have been accumulated to date. These data are useful for understanding the main features of metal fuel irradiation behavior. However, accumulation of property data is preferred for designing commercialized fast reactor fuel. Irradiation behavior modeling also requires more data, particularly on the diffusion properties for the constituent migration model and on the mechanical properties for the fuel slug deformation model. The development of high-burnup and MA-bearing fuels will require thermodynamic assessment of multicomponent alloy systems: U–Pu–Zr plus fission products and/or MA.

Injection casting is a mature technology for fuel slug fabrication, which is cost efficient (or simple), suitable for remote operation, and capable of mass production. The United States has significant experience in injection casting of fuel slugs, even by remote

operation in a hot cell. For MA-bearing metal fuel fabrication, however, other methods such as gravity casting are now being examined from the standpoint of suppressing Am evaporation.

Steady-state irradiation, transient, and out-of-pile tests extensively performed under the IFR program have produced a great amount of knowledge about the irradiation behavior of metal fuel. A high-burnup capability was demonstrated, and a sufficient margin to fuel failure in accidental events was confirmed. Fuel behavior in severe accidents, such as in-pin axial extrusion and rapid ejection–dispersion of molten fuel alloy, was also characterized, which would enhance the safety performance of the reactor core. Recent metal fuel development activities have been devoted to MA-bearing metal fuel. In metal fuel performance, there seem to be no crucial issues so far.

For the future commercialization of metal fuel, further tests are recommended, such as in-pile TOP-simulating tests for high-burnup (>10 at.%) U–Pu–Zr fuel pins, and in-pile LOF-simulating tests, which have not been covered in the IFR program. Modeling and simulation, as well as irradiation data accumulation, is important for a better understanding of metal fuel irradiation behavior. Advanced metal fuel concepts such as lined cladding are encouraged for the development of high-performance fast reactors.

Acknowledgments

The author expresses his respect for the extensive and pioneering development of metal fuel at Argonne National Laboratory and Idaho National Laboratory in the United States from the 1960s to date. A significant part of this chapter consists of their fruitful results.

References

1. Stevenson, C. E. *The EBR-II Fuel Cycle Story*; American Nuclear Society: La Grange Park, IL, 1987.
2. Walters, L. C.; Seidel, B. R.; Kittel, J. H. *Nucl. Technol.* **1984**, 65, 179.
3. Hofman, G. L.; Walters, L. C. In *Nuclear Materials*, Part 1; Frost, B. R. T., Ed.; *Material Science and Technology, A Comprehensive Treatment*; Cahn, R. W., Haasen, P., Kramer, E. J., Eds.; VCH Verlagsgesellschaft: Weinheim, 1994; Vol. 10A, Chapter 1, pp 1–43.
4. Hofman, G. L.; Walters, L. C.; Bauer, T. H. *Prog. Nucl. Energy* **1997**, 31, 83.
5. Crawford, D. C.; Porter, D. L.; Hayes, S. L. *J. Nucl. Mater.* **2007**, 371, 202.
6. Chang, Y. I. *Nucl. Technol.* **1989**, 88, 129.

7. Till, C. E.; Chang, Y. I. Progress and status of the integral fast reactor (IFR) fuel cycle development. In *Proceedings of the International Conference on Fast Reactor and Related Fuel Cycles*, Kyoto, Japan, 28 Oct–1 Nov 1991.
8. Leggett, R. D.; Walters, L. C. *J. Nucl. Mater.* **1993**, *204*, 23.
9. Tsai, H.; Cohen, A. B.; Billone, M. C.; Neimark, L. A. In *Proceedings of the 3rd JSME/ASME Joint International Conference on Nuclear Engineering*, Kyoto, Japan, 1995; Vol. 2, p 849.
10. Bauer, T. H.; Wright, A. E.; Robinson, W. R.; Holland, J. W.; Rhodes, E. A. *Nucl. Technol.* **1990**, *92*, 325.
11. Cohen, A. B.; Tsai, H.; Neimark, L. A. *J. Nucl. Mater.* **1993**, *204*, 244.
12. Liu, Y. Y.; Tsai, H.; Billone, M. C.; Holland, J. W.; Kramer, J. M. *J. Nucl. Mater.* **1993**, *204*, 194.
13. Inoue, T.; Sakata, M.; Miyashiro, H.; Matsumura, T.; Sasahara, A.; Yoshiki, N. *Nucl. Technol.* **1991**, *93*, 206.
14. Yokoo, T.; Sakata, M.; Inoue, T.; Kang, J.; Suzuki, A. *Nucl. Technol.* **1996**, *116*, 173.
15. Carmack, W. J.; Porter, D. L.; Chang, Y. I.; et al. *J. Nucl. Mater.* **2009**, *392*, 139.
16. Ogata, T.; Nakamura, K.; Ohta, H.; Kurata, M.; Yokoo, T. Research and development of fast reactor metal fuel by CRIEPI. In *International Conference on Fast Reactors and Related Fuel Cycles (FR'09)*, Kyoto, Japan, 7–11 Dec 2009.
17. Lee, C. B.; Lee, B. O.; Lee, C. T.; et al. Status of metallic fuel development for sodium-cooled fast reactor. In *Global 2009*, Paris, France, 6–11 Sept 2009.
18. Rough, F. A. Battelle Memorial Institute Report, BMI-1030, 1955.
19. Boucher, R.; Barthelemy, P. CEA-2531 (1964), ANL-TRANS-138; Argonne National Laboratory: Argonne, IL, 1964; translated by B. Blumenthal.
20. Argonne National Laboratory, Metallurgy Division. Annual Progress Report for 1965, ANL-7155, 1965.
21. Argonne National Laboratory, Reactor Development Progress Report, ANL-7230, 1966.
22. Kelman, L. R.; Savage, H.; Walter, C. M.; Blumenthal, B.; Dunworth, R. J.; Rhude, H. V. In *Proceedings of the 3rd International Conference on Plutonium*, London, 22–26 Nov 1965; Barns and Noble: New York, 1967; p 458.
23. Harbur, D. R.; Anderson, J. W.; Maraman, W. J. *Studies on the U-Pu-Zr Alloy System for Fast Breeder Reactor Applications LA-4512*; Los Alamos Scientific Laboratory: Los Alamos, NM, 1970.
24. Tou Loukian, Y. S.; et al. Ed. *Thermophysical Properties of Matter, Thermal Conductivity, Metallic Elements and Alloys*. IFI/Plenum: New York, 1970; Vol. I.
25. O'Boyle, D. R.; Dwight, A. E. In *Proceedings of the 4th International Conference on Plutonium and Other Actinides*, Santa Fe, NM; Material Society: New York, 1970; p 720.
26. Kittel, J. H.; Ayer, J. E.; Beck, W. N.; et al. *Nucl. Eng. Des.* **1971**, *15*, 373.
27. Argonne National Laboratory. Chemical Technology Division Annual Technical Report for 1986, ANL-87-19; 1987.
28. Takahashi, Y.; Yamawaki, M.; Yamamoto, K. *J. Nucl. Mater.* **1988**, *154*, 141.
29. Leibowitz, L.; Veleckis, E.; Blomquist, R. A.; Pelton, A. D. *J. Nucl. Mater.* **1988**, *154*, 145.
30. Takahashi, Y.; Yamamoto, K.; Ohsato, T.; Shimada, H.; Terai, T.; Yamawaki, M. *J. Nucl. Mater.* **1989**, *167*, 147.
31. Matsui, T.; Natsume, T.; Naito, K. *J. Nucl. Mater.* **1989**, *167*, 152.
32. Kurata, M.; Ogata, T.; Nakamura, K.; Ogawa, T. *J. Alloys Compd.* **1998**, *271*–273, 636.
33. Kurata, M. *Calphad* **1999**, *23*(3–4), 305–337.
34. Brandes, E. A., Ed. *Smithells Metals Reference Book*, 6th ed.; Butterworth: London, 1983.
35. Maeda, A.; Suzuki, Y.; Ohmichi, T. *J. Alloys Compd.* **1992**, *179*, L21–L24.
36. Ogata, T. *J. Nucl. Sci. Technol.* **2002**, (Suppl. 3), 675.
37. Massalski, T. B., Ed. *Binary Alloy Phase Diagrams*, 2nd ed.; ASM International: Materials Park, OH, 1990.
38. Billone, M. C.; Liu, Y. Y.; Gruber, E. E.; Hughes, T. H.; Kramer, J. M. In *Proceedings of the International Conference on Reliable Fuels for Liquid Metal Reactors*, Tucson, AZ, 7–11 Sept; American Nuclear Society: La Grange Park, IL, 1986.
39. Kurata, M.; et al. CRIEPI Report T92005; Central Research Institute of Electric Power Industry: Japan, 1992.
40. Gruber, E. E.; Kramer, J. M. In *Radiation-Induced Changes in Microstructure*; 13th International Symposium (Part I); 1987; ASTM STP 955, p 432.
41. Ogata, T.; Akabori, M.; Ogawa, T. *Measurement Test on Creep Strain Rate of Uranium-Zirconium Solid Solutions*, JAERI-Tech 96-052; Japan Atomic Energy Research Institute: Japan, 1996.
42. Robinson, S. L.; Sherby, O. D.; Armstrong, P. E. *J. Nucl. Mater.* **1973**, *46*, 293.
43. Adda, Y.; Philibert, J.; Faraggi, H. *Rev. Metall.* **1957**, *54*, 597.
44. Ogata, T.; Akabori, M.; Itoh, A.; Ogawa, T. *J. Nucl. Mater.* **1996**, *232*, 125.
45. Akabori, M.; Itoh, A.; Ogawa, T.; Ogata, T. *J. Alloys Compd.* **1998**, *271*–273, 597.
46. Adda, Y.; Mairy, C.; Andreu, J. L. *Rev. Metall.* **1960**, *57*, 550.
47. Petri, M. C.; Hins, A. G.; Sanecki, J. E.; Dayananda, M. A. *J. Nucl. Mater.* **1994**, *211*, 1.
48. Petri, C.; Dayananda, M. A. *J. Nucl. Mater.* **1997**, *240*, 131.
49. Kurata, M.; Inoue, T.; Sari, C. *J. Nucl. Mater.* **1994**, *208*, 144.
50. Sohn, Y. H.; Dayananda, M. A.; Hofman, G. L.; Strain, R. V.; Hayes, S. L. *J. Nucl. Mater.* **2000**, *279*, 317.
51. Burkes, D. E.; Fielding, R. S.; Porter, D. L.; Crawford, D. C.; Meyer, M. K. *J. Nucl. Mater.* **2009**, *389*, 458.
52. Burkes, D. E.; Fielding, R. S.; Porter, D. L. *J. Nucl. Mater.* **2009**, *392*, 158.
53. Argonne National Laboratory, Unpublished document.
54. Ogata, T.; Tsukada, T. Engineering-scale development of injection casting technology for metal fuel cycle. In *Global 2007*, Boise, ID, 9–13 Sept 2007.
55. Sato, K.; Fujioka, T.; Nakabayashi, H.; Kitajima, S.; Yokoo, T.; Inoue, T. Conceptual design on an integrated metallic fuel recycle system. In *Global 2003*, New Orleans, LA, 16–20 Nov 2003.
56. Nakagawa, T.; Ogata, T.; Tokiwai, M. *Trans. Am. Nucl. Soc.* **1989**, *60*, 315.
57. Lee, C. T.; Oh, S. J.; Ryu, H. J.; et al. Casting technology development for SFR metallic fuel. In *Global 2009*, Paris, France, 6–11 Sept 2009.
58. Meyer, M. K.; Hayes, S. L.; Carmack, W. J.; Tsai, H. *The EBR-II X501 Minor Actinide Burning Experiment*, INL/EXT-08-13835; Idaho National Laboratory: Idaho Falls, ID, 2008.
59. Meyer, M. K.; Hayes, S. L.; Carmack, W. J.; Tsai, H. *J. Nucl. Mater.* **2009**, *392*, 176.
60. Kim, Y. S.; Hofman, G. L.; Yacout, A. M. *J. Nucl. Mater.* **2009**, *392*, 164.
61. Trybus, C. L.; Sanecki, J. E.; Henslee, S. P. *J. Nucl. Mater.* **1993**, *204*, 50.

62. Trybus, C. L. *J. Nucl. Mater.* **1995**, 224, 305.
63. Ogata, T.; Mizuno, T. Directions of metal fuel development for fast reactors. In *Global 2009*, Paris, France, 6–11 Sept 2009.
64. Nakamura, K.; Ogata, T.; Kato, T.; Nakajima, K.; Arai, Y. Fabrication of metal fuel slug for an irradiation test in JOYO. In *Global 2009*, Paris, France, 6–11 Sept 2009.
65. Marsden, K. *Report on Development of Concepts for the Advanced Casting System in Support of the Deployment of a Remotely Operable Research Scale Fuel Fabrication Facility for Metal Fuel*, INL/EXT-07-12469; Idaho National Laboratory: Idaho Falls, ID, 2007.
66. Nakamura, K.; Kato, T.; Ogata, T.; Nakajima, K.; Iwai, T.; Arai, Y. U-Pu-Zr metal fuel fabrication for irradiation test at JOYO. In *International Conference on Fast Reactors and Related Fuel Cycles (FR'09)*, Kyoto, Japan, 7–11 Dec 2009.
67. Hofman, G. L.; Pahl, R. G.; Lahm, C. E.; Porter, D. L. *Metall. Trans.* **1990**, 21A, 517.
68. Pahl, R. G.; Porter, D. L.; Lahm, C. E.; Hofman, G. L. *Metall. Trans.* **1990**, 21A, 1863.
69. Pahl, R. G.; Porter, D. L.; Crawford, D. C.; Walters, L. C. *J. Nucl. Mater.* **1992**, 188, 3.
70. Beck, W. N.; Fousek, R. J.; Kittel, J. H. The irradiation behavior of high-burnup uranium-plutonium alloy prototype fuel elements; Argonne National Laboratory, Report ANL-7388, 1968.
71. Murphy, W. F.; Beck, W. N.; Brown, F. L.; Koproeski, B. J.; Neimark, L. A. Postirradiation examination of U-Pu-Zr fuel elements irradiated in EBR-II to 4.5 atomic percent burnup; Argonne National Laboratory, Report ANL-7602, 1969.
72. Ohta, H.; Yokoo, T.; Ogata, T.; et al. Irradiation experiment on fast reactor metal fuels containing minor actinides up to 7 at.% burnup. In *Global 2007*, Boise, ID, 9–13 Sept 2007.
73. Breton, L.; Garces, E.; Desjardins, S.; et al. METAPHIX-1 non-destructive PIE in the irradiated elements cell of PHENIX. In *Global 2007*, Boise, ID, 9–13 Sept 2007.
74. Ogata, T.; Nakamura, K.; Ohta, H. *Trans. ANS* **2008**, 98, 977.
75. Ohta, H.; Ogata, T.; Yokoo, T.; et al. *Nucl. Technol.* **2009**, 165, 96.
76. Ohta, H.; Ogata, T.; Yokoo, T.; et al. Post-irradiation examinations on fast reactor metal fuels containing minor actinides – fission gas release and metallurgy of ~2.5 at.% burnup fuels. In *Global 2009*, Paris, France, 6–11 Sept 2009.
77. Hilton, B. A.; Hayes, S. L.; Meyer, M. K.; Crawford, D. C.; Chang, G. S.; Ambrosek, R. The AFC-1AE and AFC-1F irradiation tests of metallic and nitride fuels for actinide transmutation. In *Global 2003*, New Orleans, LA, 16–20 Nov 2003.
78. Hilton, B. A.; Porter, D. L.; Hayes, S. L. *AFC-1 Transmutation Fuels Post-Irradiation Hot Cell Examination 4 to 8 at.% Final Report – Irradiation Experiments AFC-1B, AFC-1F and AFC-1AE*, INL/EXT-05-00785, Rev. 1; Idaho National Laboratory: Idaho Falls, ID, 2006.
79. Hilton, B. A.; Porter, D. L.; Hayes, S. L. *Trans. ANS* **2008**, 98, 773.
80. MacLean, H. J.; Hayes, S. L. Irradiation of metallic and oxide fuels for actinide transmutation in the ATR. In *Global 2007*, Boise, ID, 9–13 Sept 2007.
81. Hayes, S. L. *Irradiation of Metallic Fuels with Rare Earth Additions for Actinide Transmutation in the Advanced Test Reactor – Experiment Description for AFC-2A and AFC-2B*, INL/EXT-06-11707, Rev. 2; Idaho National Laboratory: Idaho Falls, ID, 2007.
82. Donnet, L.; Jorion, F.; Drin, N.; et al. The FUTURIX-FTA experiment in PHENIX: Status of fuel fabrication. In *Global 2005*, Tsukuba, Japan, 9–13 Oct 2005.
83. Jaecki, P.; Pillon, S.; Warrin, D.; et al. Update on the FUTURIX-FTA experiment in PHENIX. In *Global 2005*, Tsukuba, Japan, 9–13 Oct 2005.
84. Porter, D. L.; Lahm, C. E.; Pahl, R. G. *Metall. Trans.* **1990**, 21A, 1871.
85. Hofman, G. L.; Hayes, S. L.; Petri, M. C. *J. Nucl. Mater.* **1996**, 227, 277.
86. Kim, Y. S.; Hofman, G. L.; Hayes, S. L.; Sohn, Y. H. *J. Nucl. Mater.* **2004**, 327, 27.
87. Ogawa, T.; Iwai, T.; Kurata, M. *J. Less Common Met.* **1991**, 175, 59.
88. Ishida, M.; Ogata, T.; Kinoshita, M. *Nucl. Technol.* **1993**, 104, 37.
89. Kim, Y. S.; Hayes, S. L.; Hofman, G. L.; Yacout, A. M. *J. Nucl. Mater.* **2006**, 359, 17.
90. Ogata, T.; Mizuno, T. *Estimation of Linear Power to Melting of Metal Fuel*, CRIEPI Report L08001; Central Research Institute of Electric Power Industry: Japan, 2008.
91. Ogata, T.; Mizuno, T. Evaluation of linear-power-melting of fast reactor metal fuel. In *Proceedings of the American Nuclear Society 2009 Annual Meeting*, Atlanta, GA, 14–18 Jun 2009.
92. Barnes, R. S. *J. Nucl. Mater.* **1964**, 11, 135.
93. Pahl, R. G.; Wisner, R. S.; Billone, M. C.; Hofman, G. L. In *Proceedings of the International Fast Reactor Safety Meeting*, Snowbird, UT, 12–16 Aug 1990; Vol. IV, p 129.
94. Pahl, R. G.; Lahm, C. E.; Hayes, S. L. *J. Nucl. Mater.* **1993**, 204, 141.
95. Tsai, H.; Neimark, L. A. In *Proceedings of the International Conference on Design and Safety of Advanced Nuclear Power Plants*, Kyoto, Japan, 25–29 Oct 1992; p 28. 2–1.
96. Rest, J. *J. Nucl. Mater.* **1993**, 207, 192.
97. Crawford, D. C.; Hayes, S. L.; Pahl, R. G. *Trans. Am. Nucl. Soc.* **1994**, 71, 178.
98. Ogata, T.; Yokoo, T. *Nucl. Technol.* **1999**, 128, 113.
99. Yacout, A. M.; Salvatores, S.; Orechwa, Y. *Nucl. Technol.* **1996**, 113, 177.
100. Integral Fast Reactor Program Annual Progress Reports FY 1991; Argonne National Laboratory, Report ANL-IFR-169, 1992.
101. Beck, W. N.; Fousek, R. J. *Trans. Am. Nucl. Soc.* **1969**, 12, 78.
102. Betten, P. R. *Trans. Am. Nucl. Soc.* **1985**, 50, 237.
103. Bauer, T. H.; Holland, J. W. *Nucl. Technol.* **1995**, 110, 407.
104. Tsai, H. In *Proceedings of the International Fast Reactor Safety Meeting*, Snowbird, UT, 12–16 Aug 1990; Vol. II, p 257.
105. Tsai, H.; Liu, Y. Y.; Wang, D.-Y.; Kramer, J. M. In *Proceedings of the International Conference on Fast Reactor and Related Fuel Cycles*, Kyoto, Japan, 28 Oct–1 Nov 1991; Atomic Energy Society of Japan: Japan, 1991.
106. Inagaki, K.; Ogata, T. *Trans. Am. Nucl. Soc.* **2010**, 102, 831.
107. Tokiwi, M.; Yuda, R.; Ohuchi, A.; Amaya, M. *J. Nucl. Sci. Technol.* **2002**, 1(Suppl. 3), 913.
108. Keiser, D. D.; Cole, J. I. An evaluation of potential liner materials for eliminating FCCI in irradiated metallic nuclear fuel elements. In *Global 2007*, Boise, ID, 9–13 Sept 2007.
109. Ryu, H. J.; Lee, B. O.; Oh, S. J.; Kim, J. H.; Lee, C. B. *J. Nucl. Mater.* **2009**, 392, 206.
110. Yang, S. W.; Ryu, H. J.; Kim, J. H.; Lee, B. O.; Lee, C. B. *J. Nucl. Mater.* **2009**, 392, 206.

111. Batte, G. L.; Hofman, G. L. In *Proceedings of the International Fast Reactor Safety Meeting*, Snowbird, UT, Aug 12–16; 1990; Vol. IV, p 207.
112. Integral Fast Reactor Program; Annual Progress Report FY 1993, ANL-IFR-244, 1994.
113. Hofman, G. L.; Hins, A. G.; Porter, D. L.; Leibowitz, L.; Wood, E. L. Chemical interaction of metallic fuel with austenitic and ferritic stainless steel cladding. In *Proceedings of the International Conference on Reliable Fuels for Liquid Metal Reactors*, Tucson, AZ, 7–11 Sept 1986; pp 4–121.
114. Keiser, D. D., Jr.; Dayananda, M. A. *J. Nucl. Mater.* **1993**, *200*, 229.
115. Keiser, D. D., Jr.; Dayananda, M. A. *Metall. Mater. Trans.* **1994**, *25A*, 1649.
116. Keiser, D. D., Jr.; Petri, M. C. *J. Nucl. Mater.* **1996**, *240*, 51.
117. Ogata, T.; Kurata, M.; Nakamura, K.; Akabori, M.; Itoh, A. *J. Nucl. Mater.* **1997**, *250*, 171.
118. Nakamura, K.; Ogata, T.; Kurata, M.; Itoh, A.; Akabori, M. *J. Nucl. Mater.* **1999**, *275*, 246.
119. Ogata, T.; Nakamura, K.; Kurata, M.; Mignanelli, M. A. *J. Nucl. Sci. Technol.* **2000**, *37*(3), 244.
120. Nakamura, K.; Ogata, T.; Kurata, M.; Mignanelli, M. A. *J. Nucl. Sci. Technol.* **2001**, *38*(2), 112.
121. Ogata, T.; Nakamura, K.; Itoh, A.; Akabori, M. *Trans. Am. Nucl. Soc.* **2010**, *102*, 829.
122. Walter, A. E.; Reynolds, A. B. *Fast Breeder Reactors*; Pergamon: New York, 1981.
123. Bauer, T. H.; Fenske, G. R.; Kramer, J. M. Cladding failure margins for metallic fuel in the integral fast reactor. In *Proceedings of the 9th International Conference on Structural Mechanics in Reactor Technology*, Lausanne, Switzerland, 17–21 Aug 1987; Vol. C, p 31.
124. Walter, C. M.; Kelman, L. R. *J. Nucl. Mater.* **1966**, *20*, 314.
125. Betten, P. R.; Bottcher, J. H.; Seidel, B. R. *Trans. Am. Nucl. Soc.* **1983**, *45*, 300.